

Recovery of 21 cm BAO: a configuration-space correlation function analysis

ZHONGYUE ZHANG,^{1,2} KWAN CHUEN CHAN,^{1,2} SANTIAGO AVILA,³ AND BERNHARD VOS-GINÉS⁴

¹ *School of Physics and Astronomy, Sun Yat-Sen University, 2 Daxue Road, Tangjia, Zhuhai 519082, China*

² *CSST Science Center for the Guangdong-Hongkong-Macau Greater Bay Area, SYSU, Zhuhai 519082, China*

³ *Centro de Investigaciones Energéticas, Medioambientales y Tecnológicas (CIEMAT), 28040 Madrid, Spain*

⁴ *Fakultät für Physik, Universität Bielefeld, Postfach 100131, 33501 Bielefeld, Germany*

ABSTRACT

Intensity mapping (IM) represents an innovative and potent probe to cosmology. One of its prime applications is to measure the Baryonic Acoustic Oscillations (BAO) in the late universe. We study the BAO measurement by IM in configuration space using simulations, focusing on the impact of the telescope beam and foreground removal effects. Three types of correlation functions are applied to measure BAO, including the radial correlation function, multipole correlation function, and wedge correlation function. We check our pipeline against a set of IM mock catalogs, finding good agreement with the numerical results. We use the mock catalogs to look for the parameter choices that optimize the BAO constraint for the correlation function estimators. With the optimal settings, our pipeline is utilized to forecast the BAO constraint for the 21 cm IM experiments: BINGO, MeerKAT, and SKA-mid. We find that for the low redshift experiments BINGO and MeerKAT, the wedge correlation function achieves the tightest constraint for both the transverse and radial BAO. For SKA-mid, the radial correlation function and wedge correlation function deliver the tightest constraint for the radial and transverse BAO, respectively.

Keywords: (cosmology:) large-scale structure of universe

1. INTRODUCTION

21 cm intensity mapping (IM) represents a transformative, statistical approach to observational cosmology, offering a powerful probe across multiple cosmic epochs (Battye et al. 2013; Bharadwaj et al. 2001; McQuinn et al. 2006; Mao et al. 2008; Pritchard & Loeb 2008). The 21 cm radiation arises from the hyperfine spin-flip transition of the neutral hydrogen (H_I), transitioning from the the triplet electron-proton spin state to the singlet ground state. Unlike traditional galaxy surveys, which resolve and catalog individual galaxies, IM measures the aggregate 21 cm radio emission from H_I across vast angular patches on the sky. It does so by creating a low-resolution but efficient three-dimensional map of the total H_I luminosity.

During the cosmic dawn and the subsequent epoch of reionization, IM can reveal the birth and growth of the first large-scale structures. By mapping the faint 21 cm signal from these early times, it can track how the first stars and galaxies ionize their surrounding neutral gas, illuminating one of the last major phase transitions in cosmic his-

tory (Furlanetto et al. 2006; Pritchard & Loeb 2012). At lower redshifts, the neutral hydrogen probed by IM predominantly resides within galaxies. Consequently, the large-scale fluctuations in the 21 cm signal serve as an excellent tracer of the underlying cosmic web of dark matter of the post-reionization universe. This makes late-time IM a complementary and potent tool for studying contemporary large-scale structure. It provides a unique avenue to measure cosmological parameters, test models of gravity, and investigate the nature of dark energy through Baryon Acoustic Oscillations (BAO) and redshift-space distortions (Chang et al. 2008; Loeb & Wyithe 2008; Bull et al. 2015; Santos et al. 2015). Steady progress has been made in the 21 cm signal detection. The signals not only have been measured via cross correlation with the galaxy survey tracers, e.g. Chang et al. (2010); Masui et al. (2013); Anderson et al. (2018); Wolz et al. (2022); Cunnington et al. (2023); Amiri et al. (2024), direct auto correlation measurements have also been claimed (Paul et al. 2023; CHIME Collaboration et al. 2025).

In this work we focus on the measurement of BAO using IM. BAO are primordial acoustic features imprinted on the large-scale distribution of matter in the universe (Peebles & Yu 1970; Sunyaev & Zeldovich 1970). Their origin lies in the pre-recombination era, when photons and baryons

(electrons and protons) are tightly coupled in a hot, dense plasma. Within this medium, pressure waves propagate until the epoch of recombination, when atoms form and the photons decouple. This process freezes the waves, leaving a characteristic signature in the spatial arrangement of matter. The scale of this signature corresponds to the sound horizon at the drag epoch—the maximum distance these sound waves could travel, approximately 150 Mpc in standard cosmology. Since the physics governing BAO formation is linear and well-modeled within the early universe, this sound horizon scale can be calculated with high precision. Consequently, BAO serves as a robust standard ruler for cosmology, enabling precise measurements of the universe’s expansion history and geometry (e.g. Bond & Efstathiou (1984, 1987); Hu & Sugiyama (1996); Hu et al. (1997); Dodelson (2003)). Ever since its clear detection in SDSS (Eisenstein et al. 2005) and 2dFGS (Cole et al. 2005), BAO measurements have become a routine and essential component of large-scale structure analyses. They have been precisely charted across cosmic time by a succession of major large-scale structure survey analyses, providing a growing and powerful probe for constraining cosmological models (Gaztanaga et al. 2009; Beutler et al. 2011; Anderson et al. 2012; Kazin et al. 2014; Alam et al. 2017; Abbott et al. 2019; Alam et al. 2021; Abbott et al. 2022; Chan et al. 2022; Abbott et al. 2024; Adame et al. 2025; Abdul Karim et al. 2025).

Radio surveys for cosmology employ two primary measurement strategies. The first utilizes arrays of antennae functioning as an interferometer, whose angular resolution is determined by the minimum and maximum separation between its elements. However, many planned interferometric surveys are not optimized for BAO measurements. For instance, SKA will not be packed tight enough to offer high sensitivity for BAO (Santos et al. 2015). In contrast, the single-dish mode, where each antenna independently observes a large patch of sky, is well-suited for BAO science. This approach naturally provides the wide, contiguous field of view and high mapping speed needed to efficiently capture the vast scales of the BAO signal (Battye et al. 2013). For this reason, key ongoing and upcoming 21 cm IM experiments—including BINGO (Abdalla et al. 2022), MeerKAT (Santos et al. 2016), and the SKA Observatory (Square Kilometre Array Cosmology Science Working Group et al. 2020)—are strategically designed to utilize this method, offering prime opportunities to harness the BAO as a cosmological probe. The IM BAO is probably not as competitive as the measurement from galaxy surveys, but it paves the way for further IM studies in cosmology, e.g., the measurement of primordial non-Gaussianity.

However, there are two observational challenges, telescope beam effect and foreground removal effect, that can contaminate the signals. The telescope beam causes the modes to be

smoothed in the transverse direction. Because of the 21 cm signals is a few orders of magnitude smaller than the strong astrophysical foreground, aggressive cleaning is required and this also removes the long wavelength modes in the radial direction. This work studies the impact of these systematic effects on the recovery of the BAO signals via the correlation function approach. While there are numerous 21 cm IM BAO studies in Fourier space (e.g. Bull et al. (2015); Villaescusa-Navarro et al. (2017); Li et al. (2025)), only limited studies in configuration space (Kennedy & Bull 2021; Avila et al. 2022; Novaes et al. 2022). Kennedy & Bull (2021) applied the multipole correlation function to investigate the 21 cm IM BAO measurement. In Avila et al. (2022), a set of 21 cm IM simulation mocks were built and various configuration space correlation function were measured, but the BAO fitting was not performed. Here, we systematically study the recovery of the BAO through three different correlation function estimators. We first check our pipeline against the simulations of Avila et al. (2022). After verifying our pipeline, we go on to forecast the BAO constraints for various 21 cm IM experiments.

This paper is organized as follows. In Sec. 2, we review the correlation function formalism and present three types of correlation function estimators for 21 cm IM studies. Sec. 3 is devoted to the covariance of the estimators. In Sec. 4, we introduce the simulation sets for verification of the pipeline, and then describe the method used to infer the parameters. Sec. 5 presents the main results. In this section, we first use the mock catalog to look for the optimal parameter choices yielding the most robust and constraining results under various beam width and foreground removal strength. We go on to use the optimal setting to forecast the BAO constraint for the major ongoing and forthcoming 21 cm IM experiments. We conclude in Sec. 6. Unless otherwise stated, the cosmology adopted is a flat Λ CDM with cosmological parameters $\Omega_m = 0.309$, $h = 0.667$, $n_s = 0.967$, $\sigma_8 = 0.815$ (Planck Collaboration et al. 2016).

2. 21 CM CORRELATION FUNCTION STATISTICS

In this section, we first introduce the model for 21 cm IM power spectrum and correlation function, and then describe three types of correlation function used to measure the 21 cm IM clustering signal in this work.

2.1. 21 cm power spectrum

We use camb (Lewis et al. 2000) to compute the underlying nonlinear matter power spectrum implemented with the halo model fit (Smith et al. 2003). The particular halo model fit adopted is Mead et al. (2021), which, among other things, includes accurate BAO damping. BAO damping is the smearing of the BAO feature due to the large-scale velocity dispersion, and it can be approximated by a Gaussian damping

factor. In Mead et al. (2021), the damping factor is computed using the perturbation theory result from Crocche & Scoccamarro (2006). We have checked that the results are in agreement with that computed by other means such as Ivanov & Sibiriyakov (2018).

In terms of the matter power spectrum P_m , the cosmological 21 cm fluctuation power spectrum is given by

$$P_{21\text{cm}}^{\text{cosmo}}(k, z) = b_{21\text{cm}}^2(z)P_m(k, z), \quad (1)$$

where $b_{21\text{cm}}$ denotes $\bar{T}_b b_{\text{H}_I}$ with \bar{T}_b being the mean brightness temperature and b_{H_I} the H_I bias parameter. The brightness temperature can be expressed as (Battye et al. 2013)

$$\bar{T}_b = 191\text{mK} \frac{H_0(1+z)^2}{H(z)} \Omega_{\text{H}_I}(z)h, \quad (2)$$

where $H(z)$ is the Hubble parameter at z and $H_0 = 100 h \text{ km s}^{-1} \text{ Mpc}^{-1}$. The neutral hydrogen density parameter $\Omega_{\text{H}_I}(z)$ is defined to be the mean neutral hydrogen density at redshift z , normalized by the *present* critical density.

On top of the cosmological 21 cm signals, there are two important observational effects causing significant distortion to the observed signals. First, in the case of single-dish IM experiments, the telescope beam causes smearing in the transverse direction. We take the beam to be Gaussian and its effect on the Fourier mode is modeled by a Gaussian damping factor

$$B_{\text{beam}}(k_{\perp}) = \exp\left(-\frac{k_{\perp}^2 R_{\text{beam}}^2}{2}\right), \quad (3)$$

where k_{\perp} denotes wavenumber transverse to the line of sight. The width of the Gaussian beam R_{beam} is defined as (Villaescusa-Navarro et al. 2017)

$$R_{\text{beam}} = \frac{\theta_{\text{FWHM}}}{\sqrt{8 \ln 2}} r(z), \quad (4)$$

where $r(z)$ is the comoving distance to the source and θ_{FWHM} is the angular full width at half maximum of the beam, which is computed as

$$\theta_{\text{FWHM}} = \frac{\lambda}{D_{\text{dish}}}, \quad (5)$$

with λ being the redshifted 21 cm signal and D_{dish} the dish diameter.

The second distortion is related to the foreground contamination. The cosmological 21 cm signals suffer from serious foreground contamination caused by the galactic synchrotron radiation, free-free emission, and extragalactic sources. This is particularly challenging because the foreground is a few orders of magnitude higher than the signals. Fortunately, the foreground contamination is smooth in frequency, and this property is often exploited to clean the 21 cm IM map. See e.g., Wolz et al. (2014); Alonso et al. (2015); Liu & Shaw (2020); Cunnington et al. (2021) for some of the methods

proposed to mitigate the issue. However, the cleaning unavoidably removes also the smooth cosmological signals. We model the effect of the foreground removal on the Fourier modes by a damping term in Fourier space as

$$B_{\text{fg}}(k_{\parallel}) = 1 - \exp\left(-\frac{k_{\parallel}^2}{k_{\text{fg}}^2}\right), \quad (6)$$

where k_{\parallel} denotes the wavenumber along the line of sight direction and k_{fg} signifies the characteristic wavenumber that foreground removal imparts a significant effect. We parametrize k_{fg} by

$$k_{\text{fg}} = N_{\parallel} \frac{2\pi}{L_z}, \quad (7)$$

where L_z is the radial length scale of the survey, and N_{\parallel} emulates the number of fundamental modes removed by the foreground removal method. Soares et al. (2021) empirically find that $N_{\parallel} = 2$ can approximate well $N_{\text{IC}} = 4$ independent components removed by the FastICA method (Hyvarinen 1999). In this work, we thus take $N_{\parallel} = 2$.

Hence, in the presence of beam and foreground removal effect, the observed 21 cm IM power spectrum model reads

$$P_{21\text{cm}}(k_{\parallel}, k_{\perp}) = b_{21\text{cm}}^2 B_{\text{beam}}^2(k_{\perp}) B_{\text{fg}}^2(k_{\parallel}) P_m(k, z). \quad (8)$$

As in Avila et al. (2022), we do not consider the redshift space distortion effect in this work, although it is straightforward to include it.

In the first part of this work, we check our model against the simulation of Avila et al. (2022), which aim towards modeling an SKA-like survey, and here we follow their parameter choice. In the second part, we will use the survey specifications of BINGO, MeerKAT, and SKA to forecast their BAO constraints. Avila et al. (2022) considered two scenarios for the radial size of the survey: $L_z = 3450 \text{ Mpc } h^{-1}$ and $L_z = 300 \text{ Mpc } h^{-1}$, corresponding to the full SKA range $0.3 < z < 3$ and a small redshift bin $1.1 < z < 1.3$. Following Avila et al. (2022), we use two beam choices, $R_{\text{beam}} = 10$ and $38.45 \text{ Mpc } h^{-1}$, with the latter corresponding to the SKA beam and the former to a lower redshift study or a bigger dish size. In total, including the systematics-free cases, we discuss the scenarios with $R_{\text{beam}} = 0, 10, 38.45 \text{ Mpc } h^{-1}$ and $k_{\text{fg}} = 0, 0.00364, 0.0419 \text{ Mpc}^{-1} h$, respectively. As Avila et al. (2022), the mean brightness temperature \bar{T}_b is set to 0.183 mK. The H_I bias parameter b_{H_I} is taken to be 1.48, which is obtained by fitting to the isotropic correlation function from the simulation. In the second part, Ω_{H_I} and b_{H_I} are computed using the prescription in Villaescusa-Navarro et al. (2017) (Eq. 12 in that work), which are in very good agreement with the values adopted in the first part.

2.2. 21 cm correlation function model

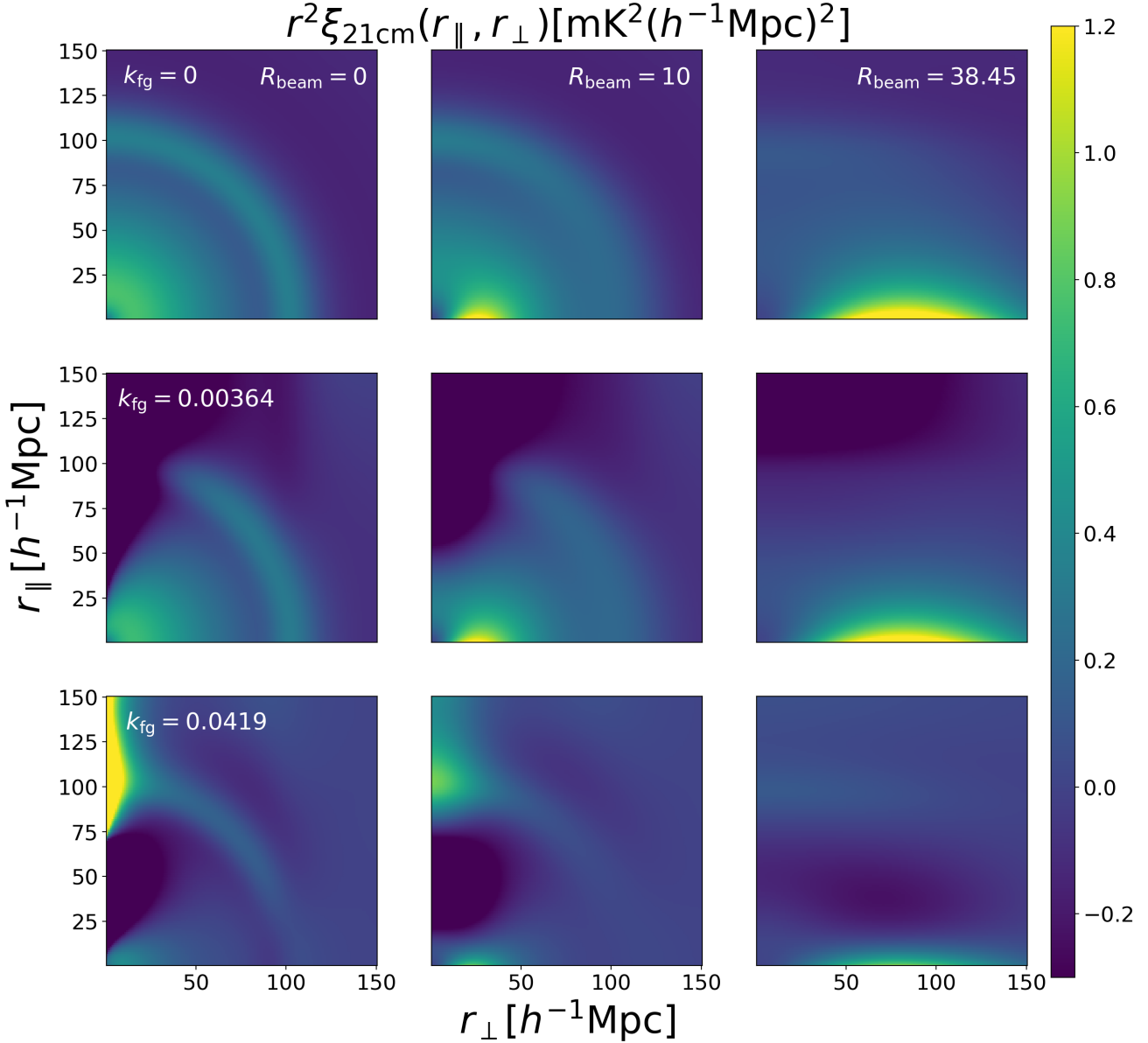


Figure 1. 2D correlation function $\xi_{21\text{cm}}$ computed with Eq. (10) for different values of R_{beam} (0, 10 and 38.45 $\text{Mpc } h^{-1}$ from left to right) and k_{fg} (0, 0.00364, 0.0419 $\text{Mpc}^{-1}h$ from top to bottom). See the text for more details.

The correlation function follows from the power spectrum by an inverse Fourier transform:

$$\xi_{21\text{cm}}(r_{\parallel}, r_{\perp}) = \int \frac{d^3k}{(2\pi)^3} e^{ik \cdot r} P_{21\text{cm}}(k_{\parallel}, k_{\perp}). \quad (9)$$

By utilizing the azimuthal symmetry of the power spectrum with respect to the line of sight, Eq. (9) becomes

$$\begin{aligned} \xi_{21\text{cm}}(r_{\parallel}, r_{\perp}) &= b_{21\text{cm}}^2 \int \frac{dk_{\parallel}}{2\pi} (1 - e^{-k_{\parallel}^2/k_{\text{fg}}^2})^2 e^{ik_{\parallel}r_{\parallel}} \\ &\times \int \frac{dk_{\perp}}{2\pi} k_{\perp} e^{-k_{\perp}^2 R_{\text{beam}}^2} J_0(k_{\perp} r_{\perp}) P_{\text{m}}(k_{\parallel}, k_{\perp}), \end{aligned} \quad (10)$$

where J_0 is the zeroth order Bessel function.

Fig. 1 showcases the 2D 21 cm IM correlation function $\xi_{21\text{cm}}$ (boosted by a factor of r^2 to highlight the BAO feature) computed with different R_{beam} (0, 10, and 38.45 $\text{Mpc } h^{-1}$) and k_{fg} (0, 0.00364, and 0.0419 $\text{Mpc}^{-1}h$) values. As R_{beam} increases, the smoothing effect increases and the BAO feature becomes more blurred. Curiously, we find that at the region close to the r_{\perp} axis, a peak appears and it shifts to larger r_{\perp} as R_{beam} increases. To shed light on this feature, we note the following closed form relation

$$\int_0^{\infty} dk_{\perp} k_{\perp} e^{-k_{\perp}^2 R_{\text{beam}}^2} J_0(k_{\perp} r_{\perp}) = \frac{1}{2R_{\text{beam}}^2} e^{-r_{\perp}^2/(4R_{\text{beam}}^2)}. \quad (11)$$

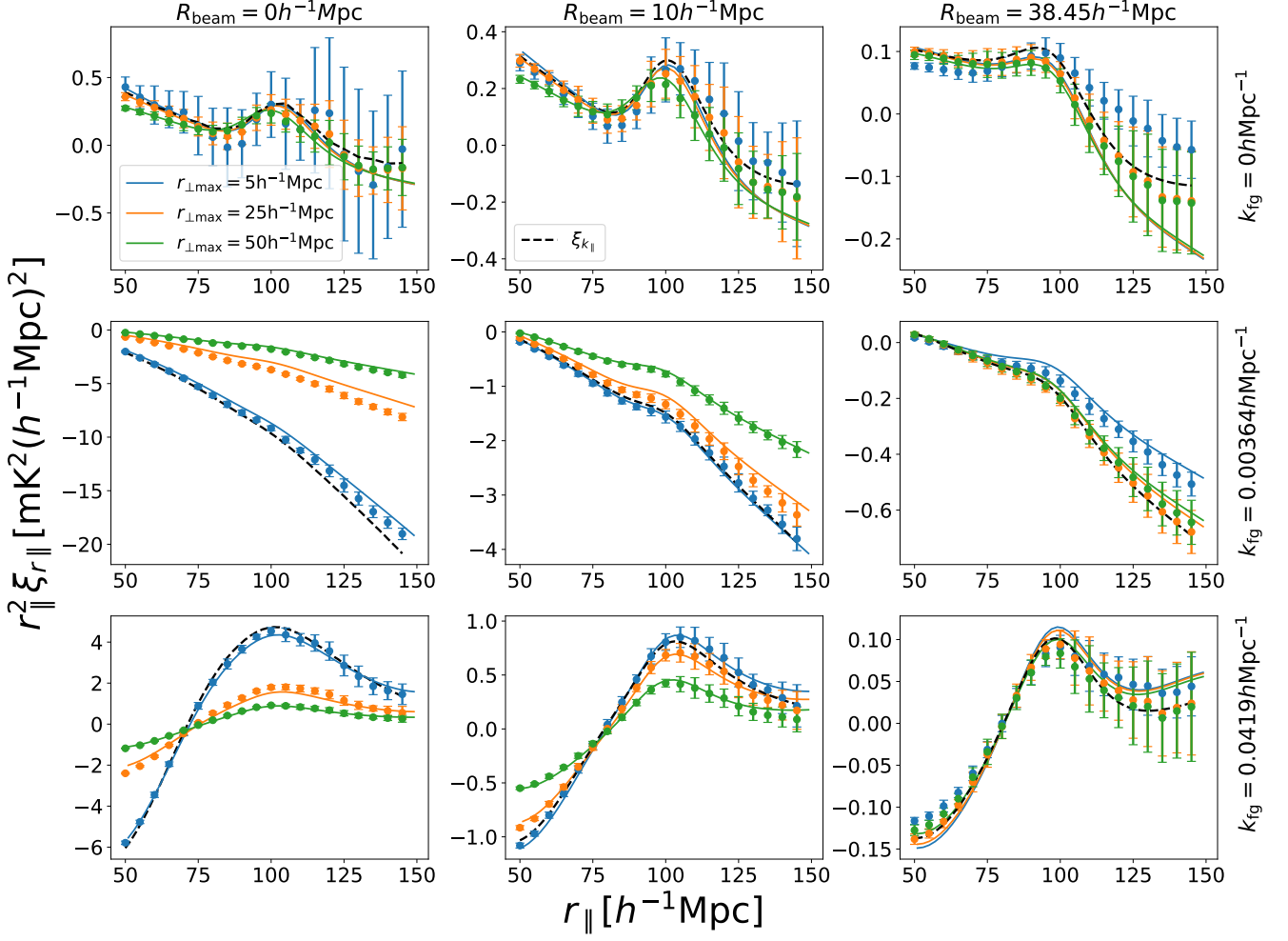


Figure 2. Radial correlation function $\xi_{r_{\parallel}}$ (color, solid) and $\xi_{k_{\parallel}}$ (black, dashed) for different values of R_{beam} (0, 10 and 38.45 $\text{Mpc } h^{-1}$ from left to right) and k_{fg} (0, 0.00364, 0.0419 $\text{Mpc}^{-1}h$ from top to bottom). The simulation measurements (markers, the error bars correspond to the standard deviation among the twelve realizations available) and the model (Eq. (16), solid lines) are compared. We have shown $\xi_{r_{\parallel}}$ obtained with $r_{\perp \text{max}} = 5$ (blue), 25 (orange), and 50 (green) $\text{Mpc } h^{-1}$, respectively.

When R_{beam} increases, this function becomes more and more broadly distributed, and hence with the boost of r^2 , it can manifest as a peak feature. Although with P_{m} , the k_{\perp} -integral in Eq. (10) is no longer analytically integrable, this feature is expected to be inherited. Secondly, to understand that the peak is restricted to the r_{\perp} axis, i.e., $r_{\parallel} = 0$, we focus on the radial integral

$$\int dk_{\parallel} e^{ik_{\parallel}r_{\parallel}} P(\sqrt{k_{\parallel}^2 + k_{\perp}^2}). \quad (12)$$

We have neglected the B_{fg}^2 term because, as evident in Fig. 1, this does not qualitatively change the feature. Applying the argument that the integral is highly oscillatory and hence large cancellation results except for $r_{\parallel} = 0$ [see similar argument in Dodelson (2003)], we conclude that the feature is significant only on the r_{\perp} -axis. Alternatively, from the uncertainty relation, the spread in configuration space is related the width of P in Fourier space, Δk_{\parallel} , as $\Delta r_{\parallel} \sim 1/\Delta k_{\parallel}$.

As k_{fg} increases, color bands show up, predominantly along the r_{\parallel} -axis. The factor B_{fg} is a high pass filter, which keeps the small-scale information and suppresses the large-scale one. Moreover, this cut-off in Fourier space also leads to oscillations in the correlation function. The trough band in the case of $k_{\text{fg}} = 0.00364 \text{ Mpc}^{-1}h$ and the trough and peak for $k_{\text{fg}} = 0.0419 \text{ Mpc}^{-1}h$ are the consequences of this oscillatory behavior. The reason that this oscillatory patterns are only apparent close to the r_{\parallel} region is because B_{fg} only suppresses the modes with $k_{\parallel} \lesssim k_{\text{fg}}$, and this is significant only if k_{\perp} is also at the similar order, i.e., $k_{\perp} \lesssim k_{\text{fg}}$. Together with the fact that $J_0(k_{\perp}r_{\perp})$ is significant for modes satisfying $k_{\perp} \sim 1/r_{\perp}$, we conclude that the bands appear around $r_{\perp} \sim 1/k_{\text{fg}}$. We indeed see that as k_{fg} increases, the characteristic r_{\perp} scale of the bands decreases.

2.3. Three types of correlation functions

From Fig. 1, it is clear that the beam and foreground cleaning introduce strong anisotropies. Isotropic correlation function alone is no longer effective for BAO measurement. To optimize the BAO extraction from the observed 21 cm IM clustering signals, we consider three types of correlation function tailored to the 21 cm IM anisotropies, as in Avila et al. (2022).

2.3.1. Radial correlation function

To deal with the strong smoothing effect in the transverse direction induced by the beam, Villaescusa-Navarro et al. (2017) proposed the radial power spectrum for 21 cm IM BAO measurement:

$$P_{\parallel}(k_{\parallel}) = \int \frac{d^2 k_{\perp}}{(2\pi)^2} P_{21\text{cm}}(k_{\parallel}, k_{\perp}). \quad (13)$$

By construction, the transverse modes are integrated out, only the radial ones left. Upon inverse Fourier transform, we get the corresponding radial correlation function

$$\xi_{k_{\parallel}}(r_{\parallel}) = \int \frac{dk_{\parallel}}{2\pi} e^{ik_{\parallel}r_{\parallel}} \int \frac{dk_{\perp}}{2\pi} k_{\perp} P_{21\text{cm}}(k_{\parallel}, k_{\perp}). \quad (14)$$

Alternatively, we can construct a radial correlation function by averaging over the correlation function up to some maximum transverse scale, $r_{\perp\text{max}}$ (Avila et al. 2022):

$$\xi_{r_{\parallel}}(r_{\parallel}; r_{\perp\text{max}}) = \frac{1}{r_{\perp\text{max}}^2} \int_0^{r_{\perp\text{max}}} dr_{\perp} 2r_{\perp} \xi_{21\text{cm}}(r_{\parallel}, r_{\perp}). \quad (15)$$

Using the relation $\int dx J_0(x) = x J_1(x)$, Eq. (15) can be expressed as

$$\begin{aligned} \xi_{r_{\parallel}}(r_{\parallel}; r_{\perp\text{max}}) &= \frac{2}{r_{\perp\text{max}}} \int \frac{dk_{\parallel}}{2\pi} e^{ik_{\parallel}r_{\parallel}} \int \frac{dk_{\perp}}{2\pi} \\ &\quad \times J_1(k_{\perp} r_{\perp\text{max}}) P_{21\text{cm}}(k_{\parallel}, k_{\perp}), \end{aligned} \quad (16)$$

where J_1 is the first order Bessel function.

One reason against using a very large $r_{\perp\text{max}}$ is that if we take $r_{\perp\text{max}}$ to infinity, then we get

$$\begin{aligned} \xi_{r_{\parallel}}(r_{\parallel}) &= \frac{1}{A} \int d^2 r_{\perp} \xi_{21\text{cm}}(r_{\parallel}, r_{\perp}) \\ &= \frac{1}{A} \int \frac{dk_{\parallel}}{2\pi} e^{ik_{\parallel}r_{\parallel}} P_{21\text{cm}}(k_{\parallel}, k_{\perp} = 0), \end{aligned} \quad (17)$$

where A is the (irrelevant) transverse area normalization. The keypoint is that the resultant correlation only depends on the power spectrum at $k_{\perp} = 0$, and this does not seem to be effective use of information.

On the other hand, from Eqs. (14) and (16), we find that they are similar in form, with $\xi_{r_{\parallel}}$ having an additional factor of the jinc function (or sombrero function)

$$\text{jinc}(k_{\perp} r_{\perp\text{max}}) \equiv \frac{2J_1(k_{\perp} r_{\perp\text{max}})}{k_{\perp} r_{\perp\text{max}}}, \quad (18)$$

which tends to unity as the argument $k_{\perp} r_{\perp\text{max}}$ approaches 0. This implies that for small $r_{\perp\text{max}}$, these two statistics are equivalent. Thus we can regard $r_{\perp\text{max}}$ as a knob controlling the range of k_{\perp} that the power spectrum is averaged over. Taking an intermediate value of $r_{\perp\text{max}}$ can be interpreted as averaging up to some intermediate $k_{\perp\text{max}}$ scale in Fourier space.

Fig. 2 shows the radial correlation function $\xi_{r_{\parallel}}$ for different values of $r_{\perp\text{max}}$: 5, 25, and 50 $\text{Mpc } h^{-1}$. We also show the $\xi_{k_{\parallel}}$ prediction, which is closest to the $\xi_{r_{\parallel}}$ result with $r_{\perp\text{max}} = 5 \text{ Mpc } h^{-1}$. The BAO feature appears to be the strongest for $r_{\perp\text{max}} = 5 \text{ Mpc } h^{-1}$. It is important to remember that this takes only the signals into account, but in reality the signal-to-noise counts. We shall compare the BAO constraint obtained from different $r_{\perp\text{max}}$ values in Sec. 5.1. We note that the $k_{\text{fg}} = 0.00364 \text{ Mpc}^{-1} h$ cases seem to be distinct from the other two k_{fg} cases. Inspection of Fig. 1 reveals that this is caused by the strong dark band, which suppresses the correlation function around the BAO scale.

2.3.2. Multipole correlation function

While the radial correlation function keeps only the radial degrees of freedom, the multipole correlation functions in principle can retain the full anisotropic clustering information. The multipole correlation function is defined as

$$\xi_l(r) = \frac{2l+1}{2} \int_{-1}^1 d\mu \xi_{21\text{cm}}(r, \mu) \mathcal{L}_l(\mu), \quad (19)$$

where $\mu \equiv r_{\parallel}/r$ and \mathcal{L}_l represents the l th order Legendre polynomial. Conversely, the correlation function can be built from the multipoles as

$$\xi_{21\text{cm}}(r, \mu) = \sum_{l=0}^{\infty} \xi_l(r) \mathcal{L}_l(\mu). \quad (20)$$

The multipole correlations are commonly employed in the anisotropic galaxy clustering, in which the anisotropies are caused by the redshift space distortion and the Alcock-Paczynski effect, and up to the quadrupole is often sufficient to capture the anisotropic information. Because of the strong anisotropies due to the telescope beam and foreground removal effect, Kennedy & Bull (2021) advocated the usage of the multipole correlation function for 21 cm IM BAO measurement.

In Fig. 3, we show the monopole ($l = 0$), quadrupole ($l = 2$), and hexadecapole ($l = 4$) correlation functions for various values of R_{beam} and k_{fg} . When $R_{\text{beam}} = 0 \text{ Mpc } h^{-1}$ and $k_{\text{fg}} = 0 \text{ Mpc}^{-1} h$, i.e., the isotropic case, all the BAO information is concentrated in the monopole. When the values of R_{beam} and k_{fg} are cranked up, some BAO information passes to the higher order multipoles. The BAO signals become progressively smaller as l increases. When R_{beam} reaches $38.45 \text{ Mpc } h^{-1}$, the BAO signature is barely visible in the multipoles.

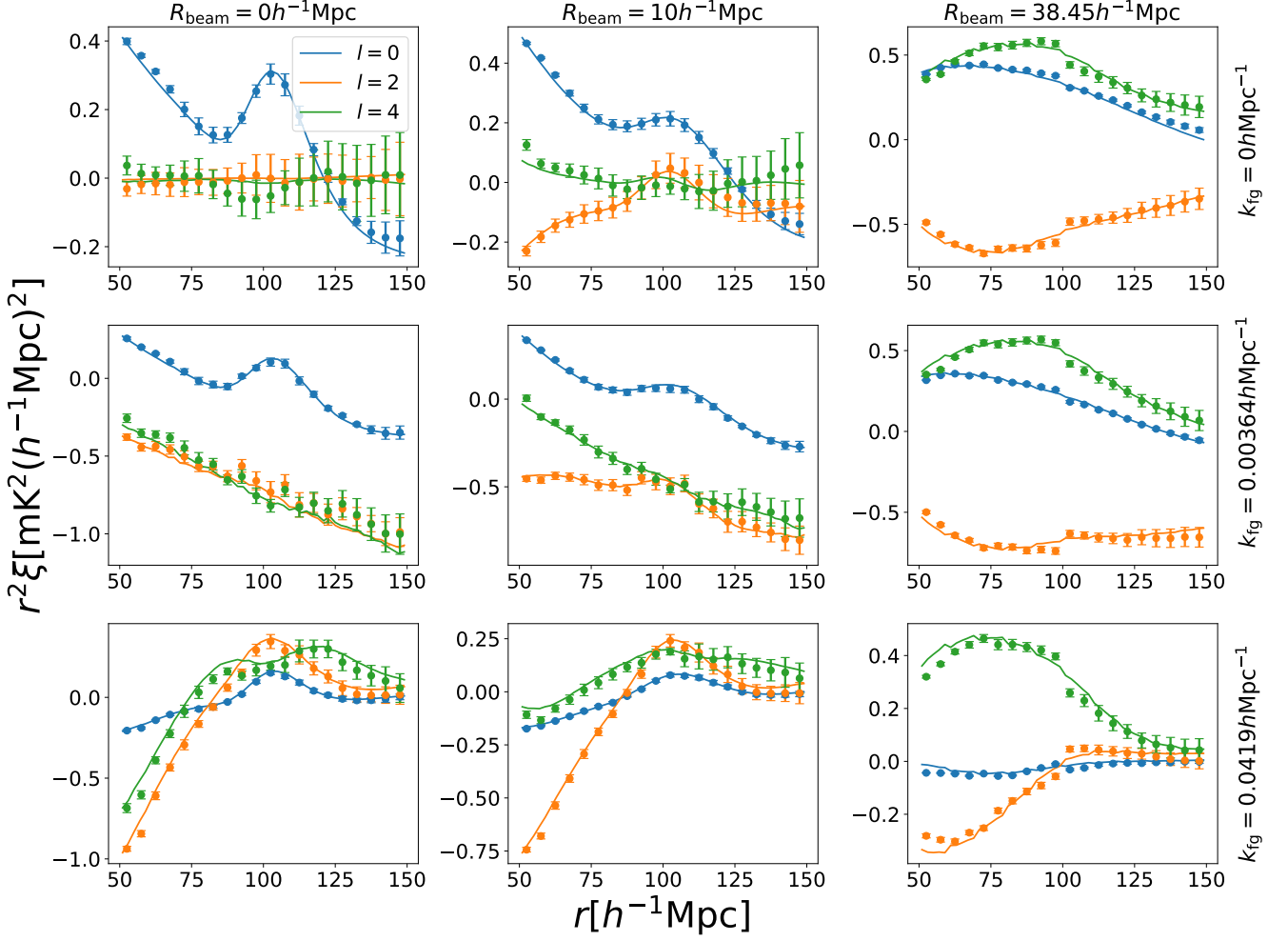


Figure 3. Multipole correlation function ξ_l for different values of R_{beam} (0, 10 and 38.45 $\text{Mpc } h^{-1}$ from left to right) and k_{fg} (0, 0.00364, 0.0419 $\text{Mpc}^{-1}h$ from top to bottom). The results from simulation measurements (markers, the error bars correspond to the standard deviation among the twelve realizations available) and model (Eq. (19), solid lines) are compared. Monopole ($l = 0$, blue), quadrupole ($l = 2$, orange), and hexadecapole ($l = 4$, green) results are displayed.

2.3.3. μ -wedge correlation function

Like the multipole correlation function, the μ -wedge correlation function is also capable of retaining the full anisotropic information, and is often employed in anisotropic galaxy clustering analysis (Sánchez et al. 2013). In this case it allows the avoidance of the strong distortion caused by the Finger-of-God along the line-of-sight direction in redshift space. To bypass the large distortion along and transverse to the line of sight direction in $\xi_{21\text{cm}}$, Avila et al. (2022) proposed the μ -wedge correlation function

$$\xi_{\mu_1, \mu_2}(r) = \frac{1}{\mu_2 - \mu_1} \int_{\mu_1}^{\mu_2} d\mu \xi_{21\text{cm}}(r, \mu), \quad (21)$$

to characterize the anisotropic correlation function. The limits μ_1 and μ_2 were chosen to avoid the features due to the beam and foreground removal effect. In general, these non-cosmological artifacts are hard to model, a simple strategy is

to avoid them altogether. To enhance the signal-to-noise, we will consider the μ -wedge correlation function refined into a number of bins.

We plot the μ -wedge correlation function in Fig. 4. We have divided the quadrant $[0, 90]^\circ$ into five bins, each of equal angular bin width. For clarity, we only show the first, third, and last bin results. We note that for the first and last bin, the models are often not in very good agreement with the measurement. This is due to the artifacts caused by the beam and foreground removal effects, and they localized in the region close to $\mu \sim 0$ and ~ 1 , respectively. We will consider getting rid of these problematic regions in the fitting.

3. CORRELATION FUNCTION COVARIANCES

To perform the BAO fit, besides the correlation function model, we also require its covariance. For a correlation func-

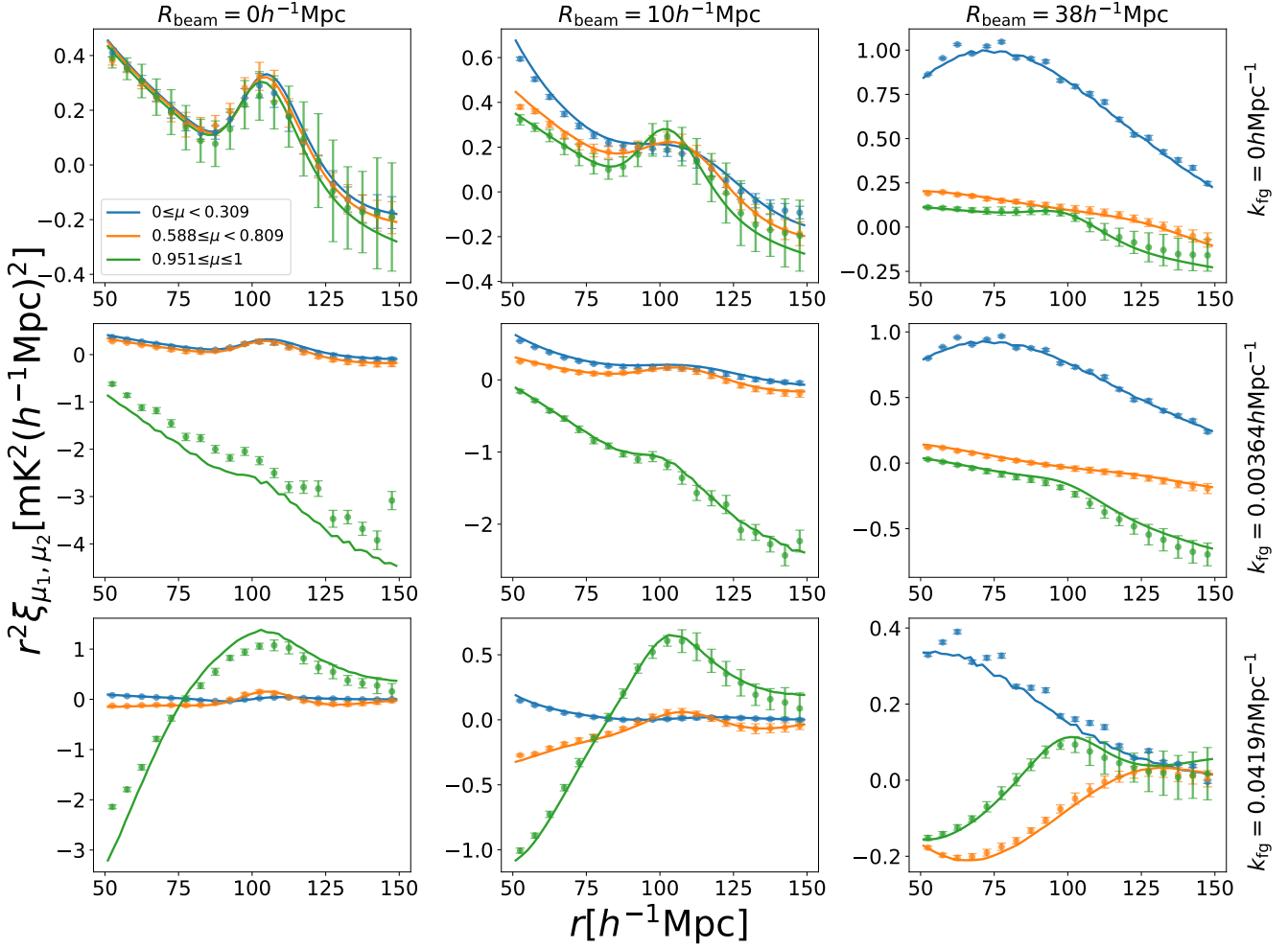


Figure 4. μ -wedge correlation function ξ_{μ_1, μ_2} for different values of R_{beam} (0, 10 and 38.45 $\text{Mpc } h^{-1}$ from left to right) and k_{fig} (0, 0.00364, 0.0419 $\text{Mpc}^{-1} h$ from top to bottom). The simulation measurements (markers, the error bars correspond to the standard deviation among the twelve realizations available) and model (Eq. (21), solid lines) are compared. The angular range $[0, 90]^\circ$ are divided into five bins with equal angular width, and for clarity, we only show the results for the first (blue), third (orange), and last (green) bin.

tion estimator $\hat{\xi}(\mathbf{r})$, its covariance is defined as

$$C(\mathbf{r}, \mathbf{r}') = \langle \hat{\xi}(\mathbf{r}) \hat{\xi}(\mathbf{r}') \rangle - \langle \hat{\xi}(\mathbf{r}) \rangle \langle \hat{\xi}(\mathbf{r}') \rangle. \quad (22)$$

In this work, we adopt the Gaussian theory covariance.

The Gaussian covariance for $\xi_{21\text{cm}}$ is given by

$$C_{21\text{cm}}(\mathbf{r}, \mathbf{r}') = \frac{1}{V} \int \frac{d^3 k}{(2\pi)^3} (P_{21\text{cm}}(\mathbf{k}) + P_N)^2 \times [e^{i\mathbf{k} \cdot (\mathbf{r} - \mathbf{r}')} + e^{i\mathbf{k} \cdot (\mathbf{r} + \mathbf{r}')}], \quad (23)$$

where V either is the simulation volume or the survey volume. In the case of galaxy clustering, P_n usually represents the Poisson shot noise and it can be written in terms of the number density of the galaxy sample, \bar{n} as $P_N = 1/\bar{n}$. For 21 cm IM clustering, the instrumental noise is the main source of noise. We can absorb this white noise contribution into P_N using an effective \bar{n} (or \bar{n}/\bar{T}_b^2 because in the convention of radio clustering, the power spectrum carries an additional

factor of \bar{T}_b^2) (Villaescusa-Navarro et al. 2017; Kennedy & Bull 2021). The Poisson noise due to the system temperature T_{sys} is given by

$$P_N = T_{\text{sys}}^2 \frac{A_{\text{sky}} \lambda_{21\text{cm}} [(1+z)r]^2}{2N_{\text{dish}} t_{\text{tot}} H(z)}, \quad (24)$$

where A_{sky} is the sky area in steradian, c is the light speed, t_{tot} is the total integration time, $\lambda_{21\text{cm}}$ is the wavelength of the rest-frame 21 cm signal, and N_{dish} is the number of dishes. This additional factor of 2 in the denominator is due to the two polarizations assumed. This white noise contribution can be derived from radiometer equation (Thompson et al. 2017), see, for example, Villaescusa-Navarro et al. (2017). For the tests in the first part, we use a fixed value of $P_N = 30 (\text{mK})^2 (\text{Mpc } h^{-1})^3$, which is in the order of magnitude expected in usual 21 cm experiments, and in the second forecast part, the value is computed based on the survey specifications.

In the following, we present the Gaussian covariance for the three types of correlation function introduced. These covariances can be viewed as different filtering or projection of the full covariance, Eq. (23).

3.1. Radial correlation function covariance

We first derive the $\xi_{k_{\parallel}}$ covariance and then discuss the $\xi_{r_{\parallel}}$ covariance at the end. Plugging in the estimator for $\xi_{k_{\parallel}}$

$$\hat{\xi}_{k_{\parallel}}(r_{\parallel}) = \int \frac{dk_{\parallel}}{2\pi} e^{ik_{\parallel}r_{\parallel}} \int \frac{d^2k_{\perp}}{(2\pi)^2} \frac{\delta_{21\text{cm}}(\mathbf{k})\delta_{21\text{cm}}(-\mathbf{k})}{V}, \quad (25)$$

with $\delta_{21\text{cm}}$ being the 21 cm IM fluctuation in Fourier space, it is easy to write down its Gaussian covariance:

$$C_{k_{\parallel}}(r_{\parallel}, r'_{\parallel}) = \frac{2}{V} \int \frac{dk_{\parallel}}{2\pi} e^{ik_{\parallel}(r_{\parallel}-r'_{\parallel})} \int \frac{d^2k_{\perp}}{(2\pi)^2} \times (P_{21\text{cm}}(k_{\parallel}, k_{\perp}) + P_{\text{N}})^2. \quad (26)$$

In the computation of covariance, it is necessary to account for the fact that the measured value is averaged within a finite bin width. We consider a bin centering at r_{\parallel} with width Δ , i.e., $[r_{\parallel} - \Delta/2, r_{\parallel} + \Delta/2]$. We first notice that

$$\frac{1}{\Delta} \int_{r_{\parallel}-\Delta/2}^{r_{\parallel}+\Delta/2} d\rho e^{ik_{\parallel}\rho} = e^{ik_{\parallel}r_{\parallel}} \text{sinc}\left(\frac{k_{\parallel}\Delta}{2}\right), \quad (27)$$

where $\text{sinc}x \equiv \sin x/x$. Thus, by averaging over the r_{\parallel} and r'_{\parallel} bins, we have

$$C_{k_{\parallel}}(r_{\parallel}, r'_{\parallel}) = \frac{2}{V} \int \frac{dk_{\parallel}}{2\pi} e^{ik_{\parallel}(r_{\parallel}-r'_{\parallel})} \text{sinc}^2\left(\frac{k_{\parallel}\Delta}{2}\right) \times \int \frac{d^2k_{\perp}}{(2\pi)^2} (P_{21\text{cm}}(k_{\parallel}, k_{\perp}) + P_{\text{N}})^2. \quad (28)$$

The results can be broken down into

$$C_{k_{\parallel}}(r_{\parallel}, r'_{\parallel}) = \frac{2}{V} (S_1 + 2P_{\text{N}}S_2 + P_{\text{N}}^2S_3), \quad (29)$$

where S_1 , S_2 , and S_3 denote

$$S_1 = b_{21\text{cm}}^4 \int \frac{dk_{\parallel}}{2\pi} e^{ik_{\parallel}(r_{\parallel}-r'_{\parallel})} \text{sinc}^2\left(\frac{k_{\parallel}\Delta}{2}\right) B_{\text{fig}}^4(k_{\parallel}) \int \frac{dk_{\perp} k_{\perp}}{2\pi} \times B_{\text{beam}}^4(k_{\perp}) P_{\text{m}}^2(k_{\parallel}, k_{\perp}), \quad (30)$$

$$S_2 = b_{21\text{cm}}^2 \int \frac{dk_{\parallel}}{2\pi} e^{ik_{\parallel}(r_{\parallel}-r'_{\parallel})} \text{sinc}^2\left(\frac{k_{\parallel}\Delta}{2}\right) B_{\text{fig}}^2(k_{\parallel}) \int \frac{dk_{\perp} k_{\perp}}{2\pi} \times B_{\text{beam}}^2(k_{\perp}) P_{\text{m}}(k_{\parallel}, k_{\perp}), \quad (31)$$

$$S_3 = \frac{k_{\perp\text{max}}^2}{4\pi} \int \frac{dk_{\parallel}}{2\pi} e^{ik_{\parallel}(r_{\parallel}-r'_{\parallel})} \text{sinc}^2\left(\frac{k_{\parallel}\Delta}{2}\right). \quad (32)$$

In S_3 , $k_{\perp\text{max}}$ is the cut-off introduced in Fourier space in order to make the integral finite.

We now turn to the covariance of $\xi_{r_{\parallel}}$. Following the earlier comment that $\xi_{r_{\parallel}}$ can be derived from $\xi_{k_{\parallel}}$ by introducing an

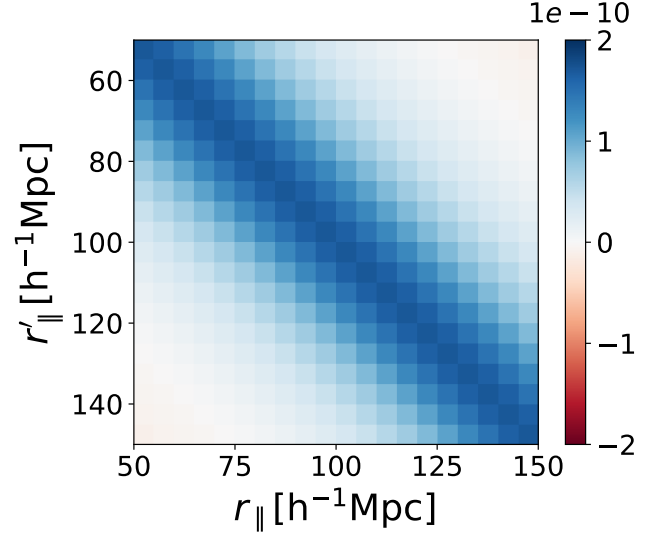


Figure 5. Radial correlation function covariance with $R_{\text{beam}} = 10 \text{ Mpc } h^{-1}$, $k_{\text{fig}} = 0.0036 \text{ Mpc}^{-1} h$, and $r_{\perp\text{max}} = 50 \text{ Mpc } h^{-1}$.

additional factor of $\text{jinc}(k_{\perp} r_{\perp\text{max}})$, we can immediately write down the corresponding covariance for $\xi_{r_{\parallel}}$:

$$C_{r_{\parallel}}(r_{\parallel}, r'_{\parallel}) = \frac{2}{V} \int \frac{dk_{\parallel}}{2\pi} e^{ik_{\parallel}(r_{\parallel}-r'_{\parallel})} \text{sinc}^2\left(\frac{k_{\parallel}\Delta}{2}\right) \int \frac{d^2k_{\perp}}{(2\pi)^2} \times \text{jinc}^2(k_{\perp} r_{\perp\text{max}}) (P_{21\text{cm}}(k_{\parallel}, k_{\perp}) + P_{\text{N}})^2. \quad (33)$$

We show a plot of the radial correlation function covariance in Fig. 5. In this plot we have taken $R_{\text{beam}} = 10 \text{ Mpc } h^{-1}$, $k_{\text{fig}} = 0.0036 \text{ Mpc}^{-1} h$, and $r_{\perp\text{max}} = 50 \text{ Mpc } h^{-1}$.

3.2. Multipole correlation function covariance

The covariance for the multipole correlation function can be written in terms of the full covariance $C(\mathbf{r}, \mathbf{r}')$ (Eq. (23)) as

$$C_{ll'}(r, r') = \frac{(2l+1)(2l'+1)}{4} \int_{-1}^1 d\mu \int_{-1}^1 d\mu' \times \mathcal{L}_l(\mu) \mathcal{L}_{l'}(\mu') C(\mathbf{r}, \mathbf{r}'). \quad (34)$$

Employing the identity

$$\int \frac{d\hat{\mathbf{r}}}{4\pi} \mathcal{L}_l(\hat{\mathbf{r}} \cdot \hat{\mathbf{n}}) e^{i\mathbf{k} \cdot \mathbf{r}} = i^l j_l(kr) \mathcal{L}_l(\hat{\mathbf{n}} \cdot \hat{\mathbf{k}}), \quad (35)$$

we can express Eq. (34) as

$$C_{ll'}(r, r') = \frac{2}{V} (2l+1)(2l'+1) i^{l+l'} \int \frac{dk k^2}{(2\pi)^2} j_l(kr) j_{l'}(kr') \times \int \frac{d\hat{\mathbf{k}}}{2\pi} \mathcal{L}_l(\hat{\mathbf{k}} \cdot \hat{\mathbf{n}}) \mathcal{L}_{l'}(\hat{\mathbf{k}} \cdot \hat{\mathbf{n}}) (P_{21\text{cm}}(k_{\parallel}, k_{\perp}) + P_{\text{N}})^2, \quad (36)$$

where $\hat{\mathbf{n}}$ denotes the line of sight direction and we have assumed even multipoles. Plugging in Eq. (8) for $P_{21\text{cm}}$, the

final expression for the multipole covariance reads (Tansella et al. 2018; Kennedy & Bull 2021)

$$C_{ll'}(r, r') = \frac{2}{V} (T_1 + P_N T_2 + P_N^2 T_3), \quad (37)$$

where these three terms are given by

$$T_1 = (2l+1)(2l'+1)l^{l+l'} b_{21\text{cm}}^4 \int \frac{dk k^2}{(2\pi)^2} j_l(kr) j_{l'}(kr') P_m^2(k) \times \int d\mu_k \mathcal{L}_l(\mu_k) \mathcal{L}_{l'}(\mu_k) B_{\text{beam}}^4(k_\perp) B_{\text{fig}}^4(k_\parallel), \quad (38)$$

$$T_2 = (2l+1)(2l'+1)l^{l+l'} b_{21\text{cm}}^2 \int \frac{dk k^2}{(2\pi)^2} j_l(kr) j_{l'}(kr') P_m(k) \times \int d\mu_k \mathcal{L}_l(\mu_k) \mathcal{L}_{l'}(\mu_k) B_{\text{beam}}^2(k_\perp) B_{\text{fig}}^2(k_\parallel), \quad (39)$$

$$T_3 = (2l+1)(2l'+1)l^{l+l'} \int \frac{dk k^2}{(2\pi)^2} j_l(kr) j_{l'}(kr') \times \int d\mu_k \mathcal{L}_l(\mu_k) \mathcal{L}_{l'}(\mu_k). \quad (40)$$

The pure shot noise term, T_3 can be computed analytically. To do so, we first note that

$$\mathcal{L}_l(\mu_k) \mathcal{L}_{l'}(\mu_k) = \sum_{L=|l-l'|}^{l+l'} \begin{pmatrix} l & l' & L \\ 0 & 0 & 0 \end{pmatrix}^2 (2L+1) \mathcal{L}_L(\mu_k), \quad (41)$$

where the big brackets denote the Wigner 3- j symbol. We can then simplify the angular integral in T_3 as

$$\begin{aligned} \int d\mu_k \mathcal{L}_l(\mu_k) \mathcal{L}_{l'}(\mu_k) &= \sum_{L=|l-l'|}^{l+l'} \begin{pmatrix} l & l' & L \\ 0 & 0 & 0 \end{pmatrix}^2 (2L+1) \int d\mu_k \mathcal{L}_L(\mu_k) \\ &= \sum_{L=|l-l'|}^{l+l'} \begin{pmatrix} l & l' & L \\ 0 & 0 & 0 \end{pmatrix}^2 (2L+1) 2\delta_{L0} \\ &= \frac{2}{2l+1} \delta_{ll'}. \end{aligned} \quad (42)$$

Moreover, we have

$$\int \frac{dk k^2}{(2\pi)^2} j_l(kr) j_{l'}(kr') = \frac{\delta_D(r-r')}{8\pi r^2}. \quad (43)$$

Consequently, T_3 can be reduced to

$$T_3 = \frac{2l+1}{4\pi r^2} \delta_{ll'} \delta_D(r-r'), \quad (44)$$

for even multipoles.

As in the radial correlation function case, we have to perform average over the bins $[r-\Delta/2, r+\Delta/2]$ and $[r'-\Delta/2, r'+\Delta/2]$. For T_1 and T_2 , this can be done by replacing j_l with its bin-averaged version \bar{j}_l :

$$\bar{j}_l(r) = \frac{1}{V(r, \Delta)} \int_{r-\frac{\Delta}{2}}^{r+\frac{\Delta}{2}} d\rho 4\pi\rho^2 j_l(\rho), \quad (45)$$

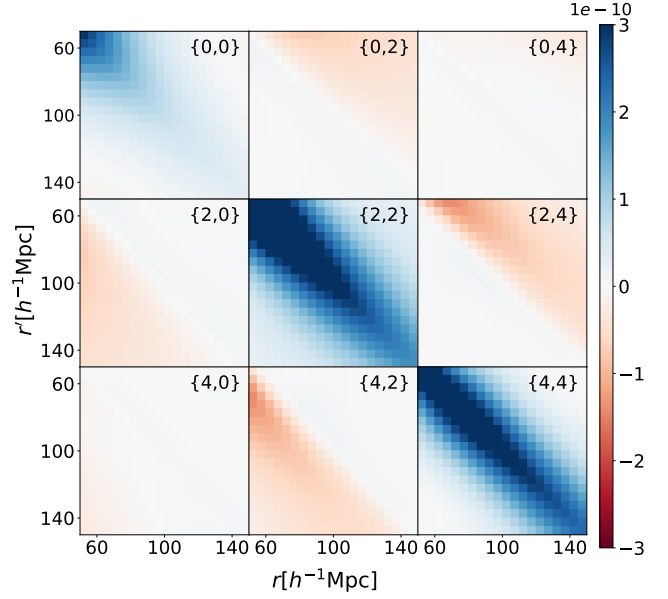


Figure 6. Multipole correlation function covariance for the monopole ($l = 0$), quadrupole ($l = 2$), and hexadecapole ($l = 4$). In this plot, we take $R_{\text{beam}} = 10 \text{ Mpc } h^{-1}$ and $k_{\text{fig}} = 0.0036 \text{ Mpc}^{-1} h$.

where $V(r, \Delta)$ is the volume of the shell

$$V(r, \Delta) = 4\pi\Delta \left(r^2 + \frac{\Delta^2}{12} \right). \quad (46)$$

Upon bin averaging, T_3 is reduced to

$$T_3 = \frac{2l+1}{4\pi r^2} \delta_{ll'} \frac{\delta_{rr'}}{\Delta}. \quad (47)$$

This result agrees with Kennedy & Bull (2021), although they did not phrase it as bin-averaging and no bin-averaging was applied in T_1 or T_2 .

In Fig. 6, we plot the multipole correlation function covariance for monopole, quadrupole, and hexadecapole. In this plot, we take $R_{\text{beam}} = 10 \text{ Mpc } h^{-1}$ and $k_{\text{fig}} = 0.0036 \text{ Mpc}^{-1} h$. The covariance of the quadrupole and hexadecapole are substantially stronger than the monopole one.

3.3. μ -wedge correlation function covariance

To compute the covariance of the μ -wedge correlation function, we first note that $\xi_{\mu_0, \mu_1}(r)$ can be expanded in terms of the multipole correlation function as

$$\xi_{\mu_1, \mu_2}(r) = \sum_l \xi_l(r) \bar{\mathcal{L}}_l(\mu_1, \mu_2), \quad (48)$$

where $\bar{\mathcal{L}}_l(\mu_1, \mu_2)$ represents the μ -averaged Legendre polynomial defined as

$$\bar{\mathcal{L}}_l(\mu_1, \mu_2) = \frac{1}{\mu_2 - \mu_1} \int_{\mu_1}^{\mu_2} d\mu \mathcal{L}_l(\mu), \quad (49)$$

which can be simplified to

$$\bar{\mathcal{L}}_l(\mu_1, \mu_2) = \begin{cases} \frac{\mathcal{L}_{l+1}(\mu_2) - \mathcal{L}_{l+1}(\mu_1) - \mathcal{L}_{l-1}(\mu_2) + \mathcal{L}_{l-1}(\mu_1)}{(2l+1)(\mu_2 - \mu_1)} & \text{if } l \geq 1, \\ 1 & \text{if } l = 0. \end{cases} \quad (50)$$

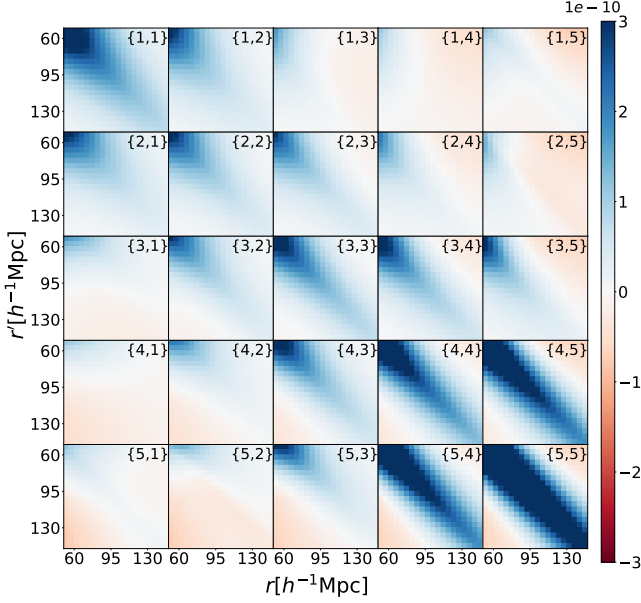


Figure 7. μ -wedge correlation function covariance for five edge case. In this plot, $R_{\text{beam}} = 10 \text{ Mpc } h^{-1}$ and $k_{\text{fg}} = 0.00364 \text{ Mpc}^{-1} h$ are used.

The covariance of the μ -wedge correlation function then reads

$$C(\xi_{\mu_1, \mu_2}(r), \xi_{\mu'_1, \mu'_2}(r')) = \sum_{l, l'} \bar{\mathcal{L}}_l(\mu_1, \mu_2) \bar{\mathcal{L}}_{l'}(\mu'_1, \mu'_2) C_{ll'}(r, r'), \quad (51)$$

where $C_{ll'}$ is given by the r -bin-averaged version of Eq. (37). We use up to $l = 30$, although for the coarse wedge setting, much fewer multipoles are required.

In Fig. 7, we show the μ -wedge covariance with $R_{\text{beam}} = 10 \text{ Mpc } h^{-1}$ and $k_{\text{fg}} = 0.00364 \text{ Mpc}^{-1} h$. As in Fig. 4, the results come from a five-wedge configuration with each wedge of equal angular width. Note that there is strong cross covariance between the neighboring bins. Moreover, the covariance of the first bin and the last two bins are stronger, which are caused by the beam and foreground removal effects, respectively.

4. METHOD

In this section, we first introduce the H_I simulation used to verify our BAO fitting pipeline, and then describe the method for parameter inference.

4.1. H_I simulation and its correlation function estimation

We utilize the H_I simulation from Avila et al. (2022). Here we present a brief overview of the simulation and refer the readers to the original paper for further details. This simulation set is built upon the UNIT N -body simulations (Chuang et al. 2019), which are dark matter only simulations in a flat Λ CDM cosmology with cosmological parameters $\Omega_m = 0.309$, $h = 0.6674$, $n_s = 0.967$, and $\sigma_8 = 0.815$.

In each simulation, there are 4096^3 particles in a cubic simulation box of volume $1 (\text{Gpc } h^{-1})^3$, resulting in the particle mass of $1.25 \times 10^9 M_\odot h^{-1}$. These simulations are run with a modified version of Gadget2 (Springel 2005). Although there are four simulations only, they are run with the fixed and paired technique (Angulo & Pontzen 2016) to reduce the covariance. The four simulations at redshift $z = 1.231$ are used. Besides, the three axes of the simulation box are rotated to generate three more sets of simulation realizations. In total, we have twelve realizations.

Halos are identified using the phase-space halo finder ROCKSTAR (Behroozi et al. 2013a), and merger trees are built with CONSISTENTTREES (Behroozi et al. 2013b) tracking halos across snapshots. From the merger history and the mass accretion history of the (sub)-halos, the Semi-Analytic Galaxy Evolution model, SAGE (Croton et al. 2016) is run in Knebe et al. (2022) to create the baryonic properties and galaxies in the halos. The model has eight free parameters, which are calibrated with a number of relations, and most of them are observational in nature. We refer the readers to Croton et al. (2016); Knebe et al. (2018) for more details on the model calibration.

To model the H_I mass in the galaxies, M_{H_I} , the cold gas mass, M_{CG} computed by SAGE is post-processed with the relation

$$M_{\text{H}_I} = f_{\text{H}} \frac{1}{1 + R_{\text{mol}}} M_{\text{CG}}, \quad (52)$$

where f_{H} is the fraction of hydrogen (set to 0.75 using the Big Bang Nucleosynthesis prediction), and $R_{\text{mol}} = M_{\text{H}_2}/M_{\text{H}_I}$ is the mass ratio between molecular hydrogen and the hydrogen atom. In Avila et al. (2022), it is taken to be a constant value, $R_{\text{mol}} = 0.4$ following Zoldan et al. (2017). We caution that there are still large uncertainties in the treatment of H_I , see the discussions in Avila et al. (2022). Consequently, the brightness temperature contrast $\Delta T = T - \bar{T}_b$ can be computed with the relation $\Delta T \propto \Delta M_{\text{H}_I} = M_{\text{H}_I} - \bar{M}_{\text{H}_I}$, using M_{H_I} obtained from SAGE.

From the temperature fluctuations ΔT , we measure the isotropic correlation function, expressed in a 2D grid as

$$\xi(r_\perp, r_\parallel) = \langle \Delta T(\mathbf{x}_\perp, \mathbf{x}_\parallel) \Delta T(\mathbf{x}_\perp + \mathbf{r}_\perp, \mathbf{x}_\parallel + \mathbf{r}_\parallel) \rangle. \quad (53)$$

We then perform a Fourier transform on $\xi(r_\perp, r_\parallel)$ by applying an FFT on r_\parallel and a Hankel transform on r_\perp . In Fourier space, we add the beam effect (Eq. (3)) and foreground removal effect (Eq. (6)), and finally perform the inverse Fourier transform to get the anisotropic correlation function in configuration space. In the computations, the voxel size is taken to be $5 \text{ Mpc } h^{-1}$, the same as Avila et al. (2022). The parameters for R_{beam} and k_{fg} are indicated at the end of Sec. 2.1.

4.2. Parameters and their inference

We describe the procedures for extracting the BAO scale from the correlation function measurement, following the standard template fitting method (e.g., Seo et al. (2012); Xu et al. (2012); Chan et al. (2018)).

The template and covariance are computed in the fiducial Planck cosmology. To accommodate any discrepancy between the fiducial model and the true data cosmology, we introduce the parameters α_{\perp} and α_{\parallel} to rescale the wavenumber in the transverse and radial direction, respectively:

$$k'_{\perp} = \frac{k_{\perp}}{\alpha_{\perp}}, \quad (54)$$

$$k'_{\parallel} = \frac{k_{\parallel}}{\alpha_{\parallel}}. \quad (55)$$

Physically, these scale dilation parameters rescale the BAO scale in the transverse and radial directions respectively

$$\alpha_{\perp} = \frac{D_M r_s^{\text{fid}}}{D_M^{\text{fid}} r_s}, \quad (56)$$

$$\alpha_{\parallel} = \frac{D_H r_s^{\text{fid}}}{D_H^{\text{fid}} r_s}, \quad (57)$$

where D_M is the comoving angular diameter distance, D_H denotes the Hubble distance $cH^{-1}(z)$, and r_s represents the sound horizon at the drag epoch. The quantities with and without “fid” mean that they are evaluated in the fiducial and the data cosmology, respectively.

As in the standard method (e.g. Seo et al. (2012); Chan et al. (2018)), the full model in real space is given by

$$\xi_{\text{model}}(r_{\perp}, r_{\parallel}) = B \xi_{\text{template}}(\alpha_{\perp} r_{\perp}, \alpha_{\parallel} r_{\parallel}) + \sum_i a_i r^i, \quad (58)$$

where ξ_{template} is the correlation function template computed using Eq. (16), (19), or (21). We include an amplitude parameter B to account for the uncertainty in $b_{21\text{cm}}$. Implicitly, ξ_{template} is a function of R_{beam} and k_{fg} as well. The broadband term $\sum_i a_i r^i$ is a polynomial in $r = \sqrt{r_{\perp}^2 + r_{\parallel}^2}$, introduced to model the potential mismatch between the broadband shape of the template and the actual measurement arising from e.g., the inadequacy in nonlinearity modeling and variation in the broadband shape due to differences in cosmologies.

We sample the posterior distribution using the MCMC sampler emcee (Foreman-Mackey et al. 2013) with the fitting parameters

$$\Theta = \{\alpha_{\perp}, \alpha_{\parallel}, R_{\text{beam}}, k_{\text{fg}}, B, a_i\}. \quad (59)$$

The data likelihood L is taken to be Gaussian

$$L \propto e^{-\chi^2/2}, \quad (60)$$

with χ^2 given by

$$\chi^2 = (\xi_{\text{data}} - \xi_{\text{model}})_i C_{ij}^{-1} (\xi_{\text{data}} - \xi_{\text{model}})_j, \quad (61)$$

where ξ_{data} and ξ_{model} denote the data and model data vectors, respectively, and C is the covariance.

The prior distribution is assumed to be uniform within some interval. The prior ranges for both α_{\perp} and α_{\parallel} are [0.7, 1.3] in all cases except R38, for which we adopt [0.5, 1.5] for α_{\perp} . The prior range for R_{beam} is within $10 \text{ Mpc } h^{-1}$ from the true value. The prior range for k_{fg} is [0, 0.01] $\text{Mpc}^{-1} h$ ([0, 0.1] $\text{Mpc}^{-1} h$) for true $k_{\text{fg}} = 0.00364 \text{ Mpc}^{-1} h$ (0.0419 $\text{Mpc}^{-1} h$). For each bin (radial bin, multipole bin, or wedge bin), we include a broadband polynomial with $i = 0$ and 1 in Eq. (59), except for the monopole bin, for which $i = 0, 1$ and 2. We perform the fitting in the range $52.5 \leq r \leq 147.5 \text{ Mpc } h^{-1}$.

5. RESULTS

In this section, we first use the mock catalog to look for the optimal settings for the three kinds of correlation functions, respectively. We then apply these statistics to forecast the parameter constraint for the ongoing and forthcoming 21 cm IM BAO experiments.

5.1. Finding the optimal parameter choices

In Table 1, we check the parameter constraint from the radial correlation function $\xi_{r\parallel}$ with $r_{\perp\text{max}} = 5, 10, 25, 50,$ and $100 \text{ Mpc } h^{-1}$, respectively. Recall that we consider the observation conditions: $R_{\text{beam}} = 0, 10, 38.45 \text{ Mpc } h^{-1}$ (denoted as R0, R10, and R38, respectively in the tables), and $k_{\text{fg}} = 0, 0.00364, 0.0419 \text{ Mpc}^{-1} h$ (denoted as k0, k1, and k2, respectively). We show the best fits and their associated $1-\sigma$ error bars. The best fit is estimated by the median of the posterior distribution, and the $1-\sigma$ error bars by the 16th and 84th percentiles, respectively. For easy inspection, the tightest constraint on α_{\parallel} is highlighted in bold. Because finite R_{beam} is required to suppress the transverse BAO modes in $\xi_{r\parallel}$, we only show $R_{\text{beam}} = 10$ and $38.45 \text{ Mpc } h^{-1}$ results. For the $k_{\text{fg}} = 0 \text{ Mpc}^{-1} h$ case, we do not consider this parameter in the model. Overall, the parameter constraint shows weak dependence on $r_{\perp\text{max}}$. The α_{\parallel} constraint tightens mildly with increasing $r_{\perp\text{max}}$, and it saturates for large $r_{\perp\text{max}}$. We find that the tightest constraints come from either $r_{\perp\text{max}} = 50$ or $100 \text{ Mpc } h^{-1}$, with no significant differences between them. For R_{beam} and k_{fg} , we also do not find clear preference for $r_{\perp\text{max}}$ values. Therefore, we take $r_{\perp\text{max}} = 50 \text{ Mpc } h^{-1}$ in the rest of the analysis.

Table 2 investigates the constraining power of the multipoles. We have contrasted the results from various combinations of the monopole ($l = 0$), quadrupole ($l = 2$), hexadecapole ($l = 4$), and hexacontatetrapole ($l = 6$). For the isotropic case, we find that the introduction of the quadrupole significantly tightens the parameter constraint, while the inclusion of the higher multipoles (hexadecapole and hexacontatetrapole) do not give further substantial improvements.

Table 1. Parameter constraints of the radial correlation function $\xi_{r\parallel}$ on the parameters α_{\parallel} , R_{beam} , and k_{fg} with different $r_{\perp\text{max}}$ values (5, 10, 25, 50, and 100 $\text{Mpc } h^{-1}$). The results obtained with various observation conditions are compared. The observation condition models are: $R_{\text{beam}} = 10, 38.45 \text{ Mpc } h^{-1}$ (denoted as R10, and R38), and $k_{\text{fg}} = 0, 0.00364, 0.0419 \text{ Mpc}^{-1}h$ (denoted as k0, k1, and k2). To guide the eyes, the constraint on α_{\parallel} with the smallest error bar is highlighted in bold.

Config.	$r_{\perp\text{max}}/\text{Mpc } h^{-1}$	α_{\parallel}	$R_{\text{beam}}/\text{Mpc } h^{-1}$	$k_{\text{fg}}/\text{Mpc}^{-1}h$
R10k0	5	0.975 ^{+0.084} _{-0.128}	12.49 ^{+5.25} _{-7.45}	–
	10	0.960 ^{+0.078} _{-0.123}	11.83 ^{+5.68} _{-7.27}	–
	25	0.967 ^{+0.070} _{-0.121}	11.50 ^{+5.95} _{-7.28}	–
	50	0.982^{+0.052} _{-0.085}	10.83 ^{+6.38} _{-7.24}	–
	100	0.974 ^{+0.062} _{-0.126}	10.76 ^{+6.46} _{-7.19}	–
R38k0	5	0.991 ^{+0.152} _{-0.170}	40.65 ^{+5.44} _{-7.17}	–
	10	0.986 ^{+0.151} _{-0.167}	40.66 ^{+5.52} _{-7.25}	–
	25	0.986 ^{+0.142} _{-0.165}	40.51 ^{+5.57} _{-7.20}	–
	50	0.985 ^{+0.126} _{-0.160}	40.50 ^{+5.56} _{-7.22}	–
	100	0.986^{+0.123} _{-0.160}	40.15 ^{+5.79} _{-7.23}	–
R10k1	5	0.969 ^{+0.0803} _{-0.120}	12.62 ^{+5.76} _{-7.36}	0.005 ^{+0.004} _{-0.003}
	10	0.966 ^{+0.076} _{-0.116}	11.95 ^{+5.55} _{-7.13}	0.005 ^{+0.004} _{-0.004}
	25	0.965 ^{+0.071} _{-0.112}	11.78 ^{+5.76} _{-7.36}	0.005 ^{+0.004} _{-0.003}
	50	0.983^{+0.051} _{-0.078}	11.11 ^{+6.23} _{-7.24}	0.005 ^{+0.004} _{-0.004}
	100	0.976 ^{+0.063} _{-0.121}	10.72 ^{+6.45} _{-7.14}	0.005 ^{+0.004} _{-0.004}
R38k1	5	0.986 ^{+0.159} _{-0.170}	40.72 ^{+5.49} _{-7.14}	0.005 ^{+0.004} _{-0.004}
	10	0.991 ^{+0.151} _{-0.167}	40.66 ^{+5.44} _{-7.10}	0.005 ^{+0.004} _{-0.004}
	25	0.985 ^{+0.143} _{-0.162}	40.39 ^{+5.54} _{-7.11}	0.004 ^{+0.002} _{-0.002}
	50	0.987 ^{+0.128} _{-0.160}	40.58 ^{+5.54} _{-7.23}	0.005 ^{+0.004} _{-0.004}
	100	0.989^{+0.121} _{-0.162}	40.39 ^{+5.67} _{-7.21}	0.005 ^{+0.004} _{-0.004}
R10k2	5	0.965 ^{+0.076} _{-0.130}	9.27 ^{+3.37} _{-3.13}	0.042 ^{+0.002} _{-0.002}
	10	0.968 ^{+0.074} _{-0.133}	9.03 ^{+3.62} _{-3.39}	0.042 ^{+0.002} _{-0.002}
	25	0.978 ^{+0.066} _{-0.116}	8.21 ^{+4.99} _{-4.52}	0.042 ^{+0.003} _{-0.003}
	50	0.988^{+0.048} _{-0.064}	8.47 ^{+6.46} _{-5.57}	0.043 ^{+0.003} _{-0.003}
	100	0.981 ^{+0.058} _{-0.080}	7.84 ^{+6.53} _{-5.21}	0.043 ^{+0.003} _{-0.003}
R38k2	5	0.987 ^{+0.156} _{-0.160}	38.62 ^{+6.52} _{-6.56}	0.045 ^{+0.009} _{-0.008}
	10	0.993 ^{+0.153} _{-0.158}	38.29 ^{+6.64} _{-6.29}	0.045 ^{+0.008} _{-0.008}
	25	0.991 ^{+0.139} _{-0.149}	38.22 ^{+6.67} _{-6.42}	0.045 ^{+0.008} _{-0.007}
	50	0.986 ^{+0.117} _{-0.137}	38.39 ^{+6.57} _{-6.64}	0.045 ^{+0.007} _{-0.006}
	100	0.990^{+0.110} _{-0.118}	38.42 ^{+6.65} _{-6.72}	0.046 ^{+0.007} _{-0.006}

The constraint on α_{\perp} is stronger than the α_{\parallel} constraint because there are more perpendicular modes available. Note that in the isotropic case, even all the information is in the monopole, however, the addition of the higher order multipoles does lead to higher information contents because of the confirmation of the vanishing of the higher order multipoles. To compare the monopole-only case with monopole plus higher order multipoles, we can think of the covariance of the higher order multipoles in the monopole-only case as infinitely large, so that they do not contribute. For the anisotropic cases due to R_{beam} or k_{fg} , $0 \oplus 2$ and $0 \oplus 2 \oplus 4$ both lead to successively tighter constraints in general, although $0 \oplus 2$ sometimes give insignificantly tighter constraint than $0 \oplus 2 \oplus 4$. Inclusion of $l = 6$ offers even less significant

Table 2. Parameter constraints for different combinations of the multipoles across various observation configurations. We have shown the results for monopole only (0), monopole and quadrupole ($0 \oplus 2$), monopole, quadrupole and hexadecapole ($0 \oplus 2 \oplus 4$), and monopole, quadrupole, hexadecapole and hexacontatetrapole ($0 \oplus 2 \oplus 4 \oplus 6$). The tightest constraints on α_{\perp} and α_{\parallel} are highlighted in bold.

Config.	Multipoles	α_{\perp}	α_{\parallel}	$R_{\text{beam}}/\text{Mpc } h^{-1}$	$k_{\text{fg}}/\text{Mpc}^{-1}h$
R0k0	0	0.986 ^{+0.055} _{-0.055}	0.986 ^{+0.123} _{-0.134}	–	–
	$0 \oplus 2$	0.998 ^{+0.033} _{-0.032}	0.996 ^{+0.054} _{-0.054}	–	–
	$0 \oplus 2 \oplus 4$	0.987^{+0.032} _{-0.032}	1.000 ^{+0.052} _{-0.053}	–	–
	$0 \oplus 2 \oplus 4 \oplus 6$	1.000^{+0.031} _{-0.033}	0.996^{+0.050} _{-0.053}	–	–
R10k0	0	0.997 ^{+0.115} _{-0.123}	1.002 ^{+0.169} _{-0.156}	10.040 ^{+5.750} _{-4.780}	–
	$0 \oplus 2$	1.000 ^{+0.112} _{-0.150}	0.983 ^{+0.104} _{-0.095}	11.960 ^{+3.350} _{-3.180}	–
	$0 \oplus 2 \oplus 4$	1.008 ^{+0.077} _{-0.115}	0.980^{+0.099} _{-0.076}	12.140 ^{+2.480} _{-2.100}	–
	$0 \oplus 2 \oplus 4 \oplus 6$	1.015^{+0.120} _{-0.082}	0.971 ^{+0.075} _{-0.101}	12.652 ^{+2.250} _{-2.038}	–
R38k0	0	0.973 ^{+0.337} _{-0.352}	0.959 ^{+0.192} _{-0.226}	42.370 ^{+4.280} _{-5.840}	–
	$0 \oplus 2$	0.995 ^{+0.331} _{-0.332}	0.963 ^{+0.172} _{-0.208}	41.220 ^{+4.790} _{-5.920}	–
	$0 \oplus 2 \oplus 4$	1.096 ^{+0.356} _{-0.275}	0.959 ^{+0.159} _{-0.157}	44.050 ^{+2.720} _{-3.120}	–
	$0 \oplus 2 \oplus 4 \oplus 6$	1.147^{+0.239} _{-0.322}	0.977^{+0.147} _{-0.164}	43.962 ^{+2.485} _{-2.677}	–
R0k1	0	1.006 ^{+0.067} _{-0.068}	0.982 ^{+0.138} _{-0.149}	–	0.005 ^{+0.004} _{-0.004}
	$0 \oplus 2$	0.998 ^{+0.037} _{-0.036}	1.001 ^{+0.072} _{-0.070}	–	0.005 ^{+0.004} _{-0.003}
	$0 \oplus 2 \oplus 4$	0.996 ^{+0.035} _{-0.035}	1.008 ^{+0.067} _{-0.064}	–	0.003 ^{+0.003} _{-0.002}
	$0 \oplus 2 \oplus 4 \oplus 6$	0.997^{+0.034} _{-0.035}	1.007^{+0.063} _{-0.065}	–	0.040 ^{+0.003} _{-0.003}
R10k1	0	0.982 ^{+0.117} _{-0.141}	1.009 ^{+0.170} _{-0.149}	10.190 ^{+5.310} _{-4.480}	0.005 ^{+0.003} _{-0.003}
	$0 \oplus 2$	1.007 ^{+0.091} _{-0.121}	0.980 ^{+0.101} _{-0.080}	12.070 ^{+4.030} _{-2.540}	0.006 ^{+0.005} _{-0.004}
	$0 \oplus 2 \oplus 4$	1.010^{+0.081} _{-0.114}	0.976^{+0.100} _{-0.080}	12.050 ^{+2.980} _{-2.320}	0.005 ^{+0.004} _{-0.003}
	$0 \oplus 2 \oplus 4 \oplus 6$	1.019 ^{+0.128} _{-0.092}	0.971 ^{+0.082} _{-0.106}	12.871 ^{+2.255} _{-2.039}	0.004 ^{+0.003} _{-0.003}
R38k1	0	1.086 ^{+0.348} _{-0.286}	0.995 ^{+0.230} _{-0.201}	43.000 ^{+3.320} _{-3.630}	0.004 ^{+0.004} _{-0.003}
	$0 \oplus 2$	0.992 ^{+0.345} _{-0.332}	0.971 ^{+0.151} _{-0.179}	46.650 ^{+5.780} _{-5.440}	0.003 ^{+0.004} _{-0.002}
	$0 \oplus 2 \oplus 4$	1.082 ^{+0.374} _{-0.287}	0.982 ^{+0.161} _{-0.164}	44.170 ^{+2.710} _{-3.450}	0.003 ^{+0.004} _{-0.002}
	$0 \oplus 2 \oplus 4 \oplus 6$	1.101^{+0.277} _{-0.367}	0.995^{+0.159} _{-0.161}	43.890 ^{+2.723} _{-2.910}	0.004 ^{+0.009} _{-0.003}
R0k2	0	1.008 ^{+0.107} _{-0.100}	0.989 ^{+0.130} _{-0.121}	–	0.041 ^{+0.010} _{-0.007}
	$0 \oplus 2$	0.998 ^{+0.066} _{-0.059}	0.996 ^{+0.061} _{-0.070}	–	0.040 ^{+0.003} _{-0.003}
	$0 \oplus 2 \oplus 4$	0.999 ^{+0.048} _{-0.052}	0.996 ^{+0.053} _{-0.053}	–	0.040 ^{+0.003} _{-0.003}
	$0 \oplus 2 \oplus 4 \oplus 6$	1.000^{+0.050} _{-0.049}	0.996^{+0.052} _{-0.051}	–	0.040 ^{+0.003} _{-0.003}
R10k2	0	1.000 ^{+0.175} _{-0.190}	1.009 ^{+0.120} _{-0.127}	9.990 ^{+5.340} _{-5.820}	0.049 ^{+0.012} _{-0.009}
	$0 \oplus 2$	1.002 ^{+0.159} _{-0.145}	0.996 ^{+0.075} _{-0.090}	9.640 ^{+3.110} _{-3.110}	0.041 ^{+0.003} _{-0.003}
	$0 \oplus 2 \oplus 4$	1.006 ^{+0.115} _{-0.132}	0.986 ^{+0.081} _{-0.080}	10.000 ^{+1.350} _{-1.110}	0.041 ^{+0.004} _{-0.003}
	$0 \oplus 2 \oplus 4 \oplus 6$	1.015^{+0.132} _{-0.104}	0.983^{+0.071} _{-0.074}	10.300 ^{+0.981} _{-1.141}	0.041 ^{+0.004} _{-0.003}
R38k2	0	0.984 ^{+0.336} _{-0.353}	0.972 ^{+0.195} _{-0.192}	39.630 ^{+6.160} _{-7.130}	0.071 ^{+0.020} _{-0.019}
	$0 \oplus 2$	0.974 ^{+0.336} _{-0.353}	0.950 ^{+0.146} _{-0.192}	45.770 ^{+5.090} _{-9.680}	0.044 ^{+0.007} _{-0.007}
	$0 \oplus 2 \oplus 4$	0.961 ^{+0.326} _{-0.355}	0.998 ^{+0.167} _{-0.166}	43.870 ^{+3.210} _{-4.650}	0.045 ^{+0.007} _{-0.006}
	$0 \oplus 2 \oplus 4 \oplus 6$	0.978^{+0.352} _{-0.327}	1.020^{+0.163} _{-0.159}	44.239 ^{+2.895} _{-3.992}	0.045 ^{+0.006} _{-0.006}

improvement, signaling that $0 \oplus 2 \oplus 4$ is already close to saturating the constraint. We choose the combination $0 \oplus 2 \oplus 4 \oplus 6$ as the fiducial setup in the rest of the analysis.

We study the impact of the μ bin division on the μ -wedge correlation function constraint in Table 3. Because the grid points of the 2D correlation function are uniformly distributed in the angular space, we choose to divide the wedge bins into equal angular bins. We divide the angular range $[\theta_{\text{min}}, \theta_{\text{max}}]$ into a number of bins, each with equal angular width of $\Delta\theta$, and concisely express it as $[\theta_{\text{min}}, \theta_{\text{max}}, \Delta\theta]$.

Let us first discuss the isotropic case. The $[0, 90, 90]^\circ$ case is equivalent to the monopole result in Table 2. Indeed, the results are similar to the monopole ones, with the differences

Table 3. Parameter constraints for different μ -wedge bin divisions. The bin division is expressed as $[\theta_{\min}, \theta_{\max}, \Delta\theta]$ degree, where θ_{\min} and θ_{\max} are the minimum and maximum angles of the μ -wedge boundaries, and $\Delta\theta$ is the angular bin width of the μ -wedges. The tightest constraints on α_{\perp} and α_{\parallel} are highlighted in bold.

Config.	bin division/ $^{\circ}$	α_{\perp}	α_{\parallel}	$R_{\text{beam}}/\text{Mpc } h^{-1}$	$k_{\text{fg}}/\text{Mpc}^{-1}h$
R0k0	[0, 90, 90]	1.017 ^{+0.051} _{-0.053}	0.997 ^{+0.118} _{-0.116}	—	—
	[0, 90, 18]	0.980 ^{+0.026} _{-0.026}	1.000 ^{+0.041} _{-0.040}	—	—
	[0, 90, 9]	0.981 ^{+0.027} _{-0.027}	1.001 ^{+0.044} _{-0.041}	—	—
	[18, 72, 18]	0.989 ^{+0.041} _{-0.042}	0.995 ^{+0.051} _{-0.051}	—	—
	[18, 72, 9]	0.990 ^{+0.039} _{-0.040}	0.994 ^{+0.050} _{-0.050}	—	—
	[18, 72, 4.5]	0.991 ^{+0.037} _{-0.038}	0.994 ^{+0.047} _{-0.048}	—	—
R10k0	[0, 90, 90]	1.018 ^{+0.121} _{-0.123}	1.007 ^{+0.162} _{-0.176}	12.00 ^{+3.35} _{-3.18}	—
	[0, 90, 18]	1.042 ^{+0.119} _{-0.083}	0.954 ^{+0.067} _{-0.089}	13.69 ^{+1.85} _{-1.87}	—
	[0, 90, 9]	1.042 ^{+0.106} _{-0.079}	0.953 ^{+0.067} _{-0.085}	13.62 ^{+1.48} _{-1.42}	—
	[18, 72, 18]	1.018 ^{+0.111} _{-0.078}	0.969 ^{+0.066} _{-0.090}	10.93 ^{+3.40} _{-2.85}	—
	[18, 72, 9]	1.012 ^{+0.105} _{-0.072}	0.968 ^{+0.064} _{-0.085}	10.56 ^{+3.28} _{-2.67}	—
	[18, 72, 4.5]	1.024 ^{+0.094} _{-0.066}	0.970 ^{+0.058} _{-0.071}	11.60 ^{+5.17} _{-2.18}	—
R38k0	[0, 90, 90]	1.106 ^{+0.270} _{-0.364}	0.942 ^{+0.244} _{-0.188}	41.20 ^{+4.97} _{-5.52}	—
	[0, 90, 18]	1.053 ^{+0.270} _{-0.278}	1.056 ^{+0.117} _{-0.108}	40.10 ^{+1.66} _{-1.82}	—
	[0, 90, 9]	1.040 ^{+0.274} _{-0.272}	1.113 ^{+0.106} _{-0.102}	38.69 ^{+1.31} _{-1.42}	—
	[18, 72, 18]	1.052 ^{+0.295} _{-0.338}	0.940 ^{+0.160} _{-0.155}	40.34 ^{+4.97} _{-6.15}	—
	[18, 72, 9]	1.033 ^{+0.300} _{-0.330}	0.955 ^{+0.150} _{-0.154}	38.79 ^{+5.34} _{-6.13}	—
	[18, 72, 4.5]	1.026 ^{+0.309} _{-0.335}	0.966 ^{+0.152} _{-0.164}	39.16 ^{+5.17} _{-6.04}	—
R0k1	[0, 90, 90]	1.013 ^{+0.104} _{-0.116}	0.970 ^{+0.194} _{-0.177}	—	0.0053 ^{+0.0036} _{-0.0029}
	[0, 90, 18]	0.975 ^{+0.027} _{-0.028}	1.009 ^{+0.041} _{-0.038}	—	0.0029 ^{+0.0006} _{-0.0004}
	[0, 90, 9]	0.985 ^{+0.025} _{-0.025}	0.994 ^{+0.034} _{-0.032}	—	0.0040 ^{+0.0007} _{-0.0005}
	[18, 72, 18]	0.992 ^{+0.043} _{-0.046}	0.989 ^{+0.053} _{-0.053}	—	0.0040 ^{+0.0016} _{-0.0016}
	[18, 72, 9]	0.994 ^{+0.044} _{-0.045}	0.985 ^{+0.053} _{-0.055}	—	0.0044 ^{+0.0017} _{-0.0014}
	[18, 72, 4.5]	0.994 ^{+0.040} _{-0.040}	0.985 ^{+0.053} _{-0.052}	—	0.0042 ^{+0.0014} _{-0.0012}
R10k1	[0, 90, 90]	1.001 ^{+0.135} _{-0.126}	1.001 ^{+0.156} _{-0.171}	10.32 ^{+5.02} _{-4.51}	0.0033 ^{+0.0025} _{-0.0023}
	[0, 90, 18]	1.023 ^{+0.118} _{-0.072}	0.971 ^{+0.058} _{-0.078}	12.29 ^{+1.50} _{-1.35}	0.0046 ^{+0.0011} _{-0.0009}
	[0, 90, 9]	0.997 ^{+0.072} _{-0.058}	0.996 ^{+0.050} _{-0.051}	11.41 ^{+0.91} _{-0.85}	0.0043 ^{+0.0008} _{-0.0006}
	[18, 72, 18]	1.020 ^{+0.121} _{-0.088}	0.964 ^{+0.070} _{-0.094}	10.69 ^{+3.02} _{-2.72}	0.0044 ^{+0.0013} _{-0.0012}
	[18, 72, 9]	1.003 ^{+0.096} _{-0.074}	0.971 ^{+0.064} _{-0.076}	10.10 ^{+2.25} _{-2.08}	0.0044 ^{+0.0011} _{-0.0009}
	[18, 72, 4.5]	1.010 ^{+0.084} _{-0.064}	0.982 ^{+0.055} _{-0.065}	10.50 ^{+1.76} _{-1.68}	0.0039 ^{+0.0008} _{-0.0007}
R38k1	[0, 90, 90]	1.097 ^{+0.278} _{-0.365}	0.945 ^{+0.234} _{-0.189}	42.86 ^{+3.86} _{-5.45}	0.0031 ^{+0.0027} _{-0.0021}
	[0, 90, 18]	0.989 ^{+0.307} _{-0.295}	1.060 ^{+0.116} _{-0.108}	40.31 ^{+1.79} _{-1.99}	0.0030 ^{+0.0015} _{-0.0014}
	[0, 90, 9]	0.958 ^{+0.320} _{-0.277}	1.111 ^{+0.105} _{-0.100}	38.81 ^{+1.41} _{-1.57}	0.0031 ^{+0.0014} _{-0.0013}
	[18, 72, 18]	1.068 ^{+0.295} _{-0.358}	0.940 ^{+0.155} _{-0.160}	42.28 ^{+4.20} _{-5.75}	0.0049 ^{+0.0032} _{-0.0023}
	[18, 72, 9]	1.076 ^{+0.290} _{-0.345}	0.942 ^{+0.161} _{-0.158}	40.97 ^{+5.49} _{-5.49}	0.0044 ^{+0.0028} _{-0.0020}
	[18, 72, 4.5]	1.066 ^{+0.294} _{-0.337}	0.946 ^{+0.159} _{-0.156}	41.24 ^{+4.49} _{-5.31}	0.0046 ^{+0.0027} _{-0.0020}
R0k2	[0, 90, 90]	1.013 ^{+0.101} _{-0.099}	1.010 ^{+0.117} _{-0.112}	—	0.0413 ^{+0.0102} _{-0.0066}
	[0, 90, 18]	0.952 ^{+0.039} _{-0.040}	1.028 ^{+0.051} _{-0.049}	—	0.0389 ^{+0.0008} _{-0.0008}
	[0, 90, 9]	1.034 ^{+0.035} _{-0.033}	0.949 ^{+0.042} _{-0.044}	—	0.0401 ^{+0.0004} _{-0.0004}
	[18, 72, 18]	0.982 ^{+0.054} _{-0.058}	1.010 ^{+0.071} _{-0.062}	—	0.0371 ^{+0.0062} _{-0.0055}
	[18, 72, 9]	0.983 ^{+0.045} _{-0.047}	1.006 ^{+0.059} _{-0.055}	—	0.0401 ^{+0.0051} _{-0.0050}
	[18, 72, 4.5]	0.980 ^{+0.046} _{-0.048}	1.005 ^{+0.059} _{-0.054}	—	0.0408 ^{+0.0050} _{-0.0050}
R10k2	[0, 90, 90]	0.991 ^{+0.125} _{-0.164}	1.015 ^{+0.125} _{-0.126}	8.97 ^{+4.22} _{-5.20}	0.0434 ^{+0.0068} _{-0.0055}
	[0, 90, 18]	0.943 ^{+0.101} _{-0.084}	1.016 ^{+0.073} _{-0.068}	10.11 ^{+0.88} _{-0.85}	0.0397 ^{+0.0015} _{-0.0014}
	[0, 90, 9]	0.935 ^{+0.092} _{-0.077}	1.029 ^{+0.070} _{-0.069}	9.73 ^{+0.84} _{-0.84}	0.0397 ^{+0.0015} _{-0.0014}
	[18, 72, 18]	1.047 ^{+0.154} _{-0.134}	0.967 ^{+0.091} _{-0.103}	11.84 ^{+1.11} _{-1.20}	0.0408 ^{+0.0031} _{-0.0031}
	[18, 72, 9]	1.005 ^{+0.138} _{-0.109}	0.985 ^{+0.081} _{-0.087}	10.24 ^{+1.97} _{-1.87}	0.0409 ^{+0.0035} _{-0.0037}
	[18, 72, 4.5]	1.039 ^{+0.133} _{-0.108}	0.956 ^{+0.070} _{-0.087}	11.25 ^{+1.02} _{-1.03}	0.0431 ^{+0.0027} _{-0.0026}
R38k2	[0, 90, 90]	0.954 ^{+0.367} _{-0.325}	0.992 ^{+0.180} _{-0.194}	35.77 ^{+8.34} _{-10.34}	0.0653 ^{+0.0128} _{-0.0130}
	[0, 90, 18]	0.998 ^{+0.351} _{-0.335}	1.008 ^{+0.157} _{-0.160}	40.53 ^{+2.26} _{-2.29}	0.0403 ^{+0.0029} _{-0.0027}
	[0, 90, 9]	0.912 ^{+0.391} _{-0.302}	1.064 ^{+0.148} _{-0.167}	38.66 ^{+1.55} _{-1.78}	0.0409 ^{+0.0032} _{-0.0028}
	[18, 72, 18]	0.990 ^{+0.340} _{-0.319}	0.981 ^{+0.169} _{-0.168}	37.96 ^{+3.44} _{-3.62}	0.0436 ^{+0.0040} _{-0.0039}
	[18, 72, 9]	1.007 ^{+0.331} _{-0.328}	0.981 ^{+0.171} _{-0.171}	38.26 ^{+3.26} _{-3.28}	0.0431 ^{+0.0039} _{-0.0037}
	[18, 72, 4.5]	1.033 ^{+0.322} _{-0.336}	0.993 ^{+0.166} _{-0.183}	40.30 ^{+2.71} _{-2.74}	0.0399 ^{+0.0036} _{-0.0033}

primarily caused by the number of broadband terms used. We then divide the angular range into five bins ($[0, 90, 18]^{\circ}$) and ten bins ($[0, 90, 9]^{\circ}$), and we find that increase of resolution does not lead to tighter constraints. To contrast with the anisotropic cases, we also show the cases $[18, 72, \Delta\theta]^{\circ}$. With the modes at both ends cut out, the constraints are weaker than the full range case. We also show the highest resolution case, $[18, 72, 4.5]^{\circ}$, whose constraint is very similar to $[18, 72, 9]^{\circ}$, showing that the constraints are already saturated at the resolution of $\Delta\theta = 9^{\circ}$.

As we noted, for the anisotropic cases, there are artifacts appearing on the x and y axis in Fig. 1 due to the beam and foreground removal effect, respectively. For the full range cases, especially $[0, 90, 9]^{\circ}$, the μ -wedge correlation function often gives tighter constraint when the resolution increases. However, we also note that occasionally the bias is substantial in the sense that the expected values lie outside the $1\text{-}\sigma$ interval. For example, in R38k0 and R0k2, $[0, 90, 9]^{\circ}$ gives the tightest but mildly biased constraint. This demonstrates that these artifacts are difficult to model well and may cause the fit to be unstable. The μ -wedge correlation function allows for the possibility to remove the artifacts on the axes. By inspection of Fig. 1, we choose to remove the intervals $[0, 18]^{\circ}$ and $[72, 90]^{\circ}$. Excision of these intervals, on one hand reduces the data size and hence enlarges the error bar, while it gives rise to more stable fit on the other hand. Overall, with the removal of the artifact regions, we find that the results are always within $1\text{-}\sigma$ from the expected value. There are no significant improvements when the bin division is refined to $[18, 72, 4.5]^{\circ}$. With these considerations in mind, we take the bin division $[18, 72, 9]^{\circ}$ as the fiducial setting for its tight parameter constraint and robustness to artifacts.

We find that the configuration $[0, 90, 9]^{\circ}$ tends to give slightly tighter constraints than the multipole combination $0 \oplus 2 \oplus 4 \oplus 6$, while the fiducial setting $[18, 72, 9]^{\circ}$ yields compatible constraints as the multipole. This suggests that the lower multipoles are also insensitive to the artifacts. This is so because the lower multipoles retain the “wide angle” fluctuations and the impact of the artifacts are suppressed as they are relatively localized.

In Fig. 8 we show the best fit contour distributions for the parameters α_{\perp} , α_{\parallel} , R_{beam} , and k_{fg} obtained with their fiducial settings. This example uses $R_{\text{beam}} = 10 \text{ Mpc } h^{-1}$ and $k_{\text{fg}} = 0.0419 \text{ Mpc}^{-1}h$. In this example, the constraints by the multipoles and μ -wedges are rather similar. Besides the mild degeneracy between α_{\perp} and α_{\parallel} , there are no strong degeneracy between the parameters, in particular, between R_{beam} and k_{fg} . While R_{beam} is well constrained by the multipoles or wedges, it is hardly constrained by the radial correlation function.

Fig. 9 visually contrasts the optimal setting results from these three statistics. The best fit results for α_{\perp} and α_{\parallel} are

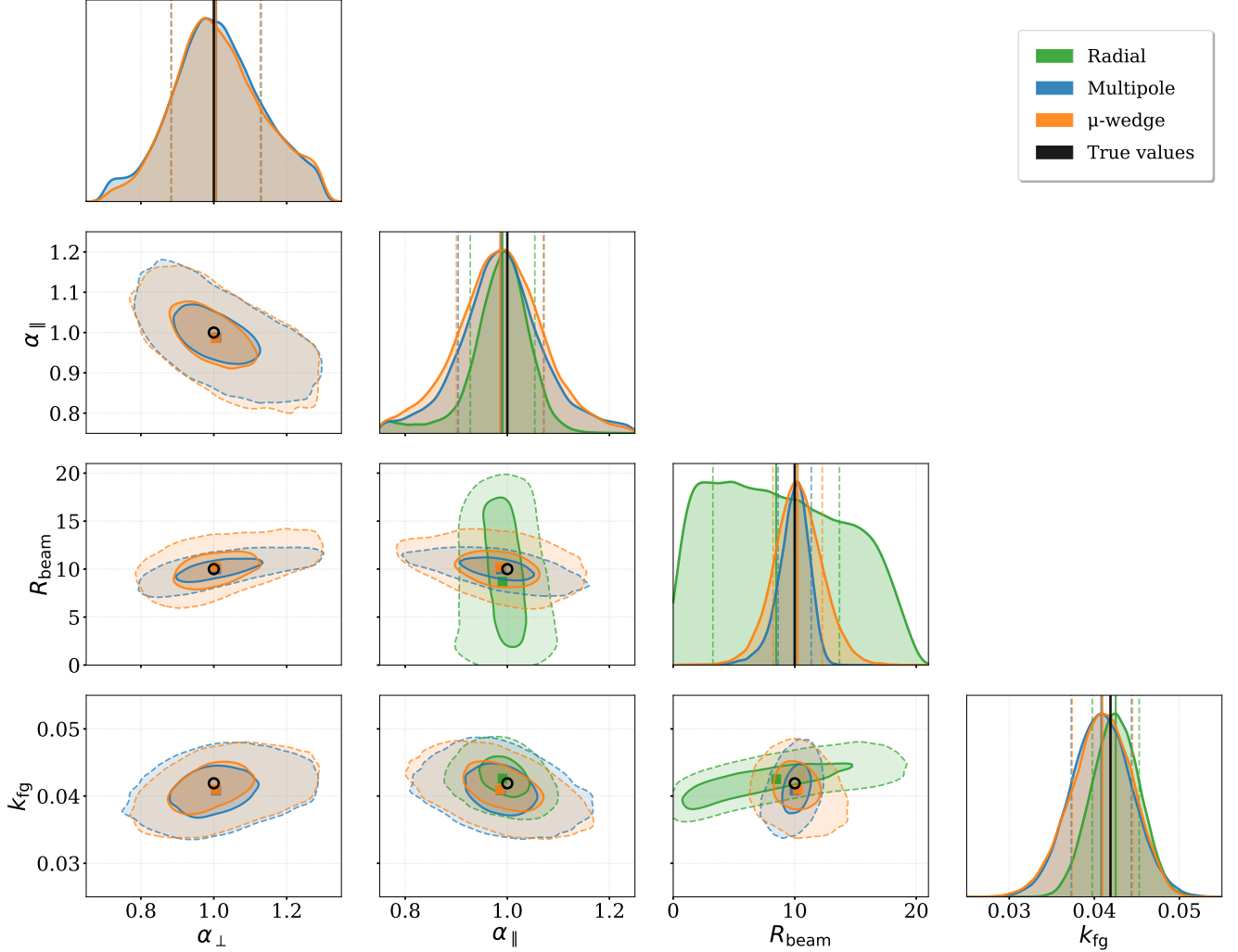


Figure 8. Corner plots for the parameters α_{\perp} , α_{\parallel} , R_{beam} , and k_{fg} . The posterior distributions for the radial correlation function (green), multipole correlation function (blue), and μ -wedge correlation function (orange) are shown. The true values are highlighted in black. The inner and outer contour curves represent the $1\text{-}\sigma$ and $2\text{-}\sigma$ distribution boundaries, respectively, and the maximum of the distribution is marked by a square marker. In the 1D marginal distribution, we show the median (solid) and the 16th and 84th percentiles (dashed).

shown across various observation conditions. Generally, the constraints become weaker when R_{beam} increases, while the trend is not apparent for the k_{fg} values considered. For both α_{\parallel} and α_{\perp} , the multipoles and μ -wedges show very comparable constraining power. $\xi_{r\parallel}$ can deliver an effective constraint on α_{\parallel} for $R \geq 10 \text{ Mpc } h^{-1}$ cases, and in fact it outperforms the others by a small margin for the k2 cases.

5.2. Survey forecasts

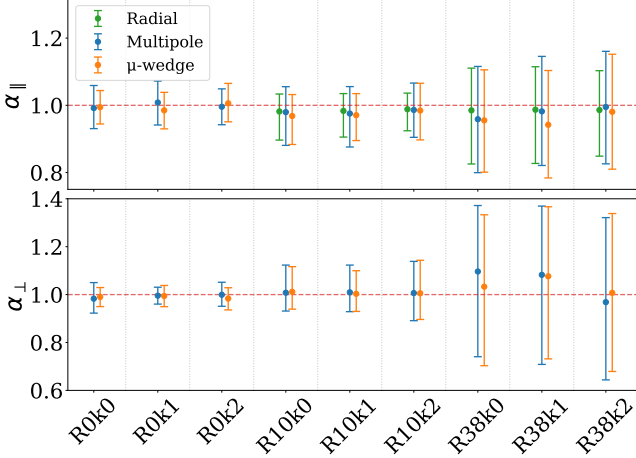
After verifying and optimizing the pipelines with the mocks, we now apply them to forecast the parameter constraints for the major ongoing and forthcoming 21 cm IM surveys. They encompass BINGO (Abdalla et al. 2022; Wuensche et al. 2022), MeerKAT (Santos et al. 2016), SKA (Braun et al. 2015; Maartens et al. 2015; Square Kilometre Array Cosmology Science Working Group et al. 2020). The key parameters of these surveys and their instruments used

for the forecasts are listed in Table 4. The pathfinding experiments BINGO and MeerKAT focus on the relatively low redshift universe, while the mean redshift and volume of the SKA are larger than its predecessors. In particular, for SKA-mid, we consider the Wide Band 1 survey setting (Square Kilometre Array Cosmology Science Working Group et al. 2020), which is an IM survey covering $20,000 \text{ deg}^2$ in the redshift range of $0.35 < z < 3$. The foreground parameter k_{fg} is computed by taking $N_{\parallel} = 2$ in Eq. (7), the same as the prescription used in the first part.

To perform the forecast, we generate a data vector using the theoretical model on a grid with spacing of $1 \text{ Mpc } h^{-1}$ and then apply the fitting pipeline to this mock data vector to get the constraint. The forecasts on the parameters are shown in Table 5. To highlight the constraints on α_{\perp} and α_{\parallel} , we present them as a function of the mean redshifts of these

Table 4. Key parameters of the major 21 cm IM surveys and their instruments used for BAO constraint forecasts.

Experiment	\bar{z}	FWHM/deg	$r(z)/\text{Mpc } h^{-1}$	$l_z/\text{Mpc } h^{-1}$	f_{sky}	T_{sys}/K	t_{tot}/h	$N_{\text{dish}} \times N_{\text{feed}}$	$R_{\text{beam}}/\text{Mpc } h^{-1}$	$k_{\text{fg}}/\text{Mpc}^{-1}h$	$P_N/(\text{mK})^2(\text{Mpc } h^{-1})^{-3}$
BINGO	0.29	0.38	800	850	0.15	70	17520	1×50	2.27	0.015	2.9
MeerKAT	0.39	1.25	1000	342	0.1	19	4000	64×1	9.85	0.037	0.9
SKA-mid	1.32	1.85	2793	3450	0.48	26	10000	197×1	38.45	0.0036	12.2

**Figure 9.** Visual representation of the best fit α_{\parallel} and α_{\perp} under various observation conditions. The results from the radial correlation function (green), multipole correlation function (blue), and μ -wedge correlation function (orange) are compared.**Table 5.** Forecasts for the BAO recovery from the major 21 cm experiments. We have shown the forecast results from three statistics using the optimal settings. The μ -wedge correlation function gives the tightest constraint.

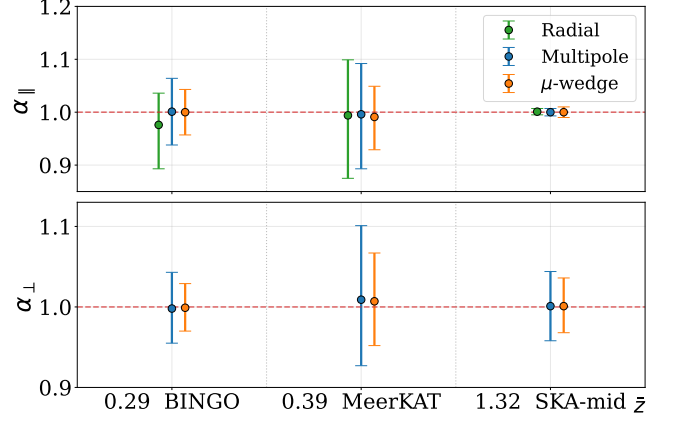
Experiment	statistics	α_{\perp}	α_{\parallel}	$R_{\text{beam}}/\text{Mpc } h^{-1}$	$k_{\text{fg}}/\text{Mpc}^{-1}h$
BINGO	Radial	–	$0.976^{+0.060}_{-0.083}$	$6.48^{+3.98}_{-4.27}$	$0.0115^{+0.0046}_{-0.0083}$
	Multipole	$0.998^{+0.045}_{-0.043}$	$1.001^{+0.063}_{-0.063}$	$2.24^{+1.36}_{-1.41}$	$0.0155^{+0.0020}_{-0.0018}$
	μ -wedge	$0.999^{+0.030}_{-0.029}$	$1.000^{+0.043}_{-0.043}$	$2.26^{+0.14}_{-0.14}$	$0.0152^{+0.0004}_{-0.0004}$
MeerKAT	Radial	–	$0.994^{+0.105}_{-0.119}$	$9.42^{+6.23}_{-6.26}$	$0.0366^{+0.0034}_{-0.0031}$
	Multipole	$1.009^{+0.092}_{-0.082}$	$0.996^{+0.096}_{-0.103}$	$9.86^{+0.64}_{-0.61}$	$0.0370^{+0.0023}_{-0.0021}$
	μ -wedge	$1.007^{+0.060}_{-0.055}$	$0.991^{+0.058}_{-0.062}$	$9.91^{+0.29}_{-0.27}$	$0.0368^{+0.0009}_{-0.0008}$
SKA-mid	Radial	–	$1.001^{+0.006}_{-0.006}$	$38.12^{+4.62}_{-4.23}$	$0.0042^{+0.0034}_{-0.0029}$
	Multipole	$1.001^{+0.043}_{-0.043}$	$1.000^{+0.007}_{-0.007}$	$38.45^{+0.14}_{-0.14}$	$0.0037^{+0.0003}_{-0.0003}$
	μ -wedge	$1.001^{+0.035}_{-0.033}$	$1.000^{+0.010}_{-0.010}$	$38.45^{+0.14}_{-0.14}$	$0.0036^{+0.0002}_{-0.0002}$

surveys in Fig. 10 as well. For the low redshift experiments BINGO and MeerKAT, the R_{beam} size is small or moderate. We find that the μ -wedge is the most effective in constraining α_{\perp} or α_{\parallel} . For SKA-mid, which has a larger R_{beam} and smaller k_{fg} , while μ -wedge still attains the strongest constraint on α_{\perp} , ξ_{\parallel} is the most constraining one for α_{\parallel} .

We wish to compare our results with others', and so we consider the total signal-to-noise, $(S/N)^2$ defined as

$$\left(\frac{S}{N}\right)^2 = \sum_i \left(\frac{\alpha_i}{\sigma_{\alpha,i}}\right)^2 \approx \sum_i \left(\frac{1}{\sigma_{\alpha,i}}\right)^2, \quad (62)$$

where the summation runs over all the tomographic bins, and α_i and $\sigma_{\alpha,i}$ denote the best fit and its error bar in the i th

**Figure 10.** Visual representation of the best fit α_{\parallel} and α_{\perp} for BINGO, MeerKAT, and SKA-mid. On the x -axis, the mean redshift of these surveys are labeled. The results from the radial correlation function (green), multipole correlation function (blue), and μ -wedge correlation (orange) are compared.

bin. This is especially useful if others' forecast is conducted in multiple tomographic bins while ours is computed at the mean redshift only.

Novaes et al. (2022) performed a BAO constraint forecast for BINGO using only the transverse information. In that study, the whole redshift range is divided into 30 fine tomographic bins and the angular correlation functions are measured. Using their fit to the mean angular correlation function (Table 2 of Novaes et al. (2022)), we get $(S/N)^2 = 178$ on α_{\perp} ¹. Our multipole and μ -wedge analysis result in $(S/N)^2$ of 516 and 1150, respectively. Moreover, we show that appreciable constraint on α_{\parallel} is also achievable by the multipoles and μ -wedges, with $(S/N)^2$ of 252 and 540, respectively. Our results thus suggest that the 3D analysis is more effective than the multibin tomographic one in both α_{\perp} and α_{\parallel} constraints.

We now turn to the MeerKAT survey. We first note that its R_{beam} and k_{fg} values are close to the R10k2 case, but there are two key differences, which are competing in BAO constraints. First, the MeerKAT redshift is lower and hence the cosmological BAO signals are weaker. Second, the value of the noise P_N is $0.9 (\text{mK})^2 (\text{Mpc } h^{-1})^3$ for MeerKAT versus $30 (\text{mK})^2 (\text{Mpc } h^{-1})^3$ assumed in R10k2. For ξ_{\parallel} and μ -wedge, we find that the constraints in MeerKAT are tighter than in R10k2 by different extents, while for the multipoles,

¹ We note that Novaes et al. (2022) also performed the angular power spectrum analysis, and it yielded instead a much higher $(S/N)^2$, 1700.

the transverse BAO constraint is tighter but the radial BAO constraint is weaker relative to R10k2. Kennedy & Bull (2021) conducted a BAO forecast for MeerKAT using the multipole correlation functions. Their error bars on α_{\perp} and α_{\parallel} are about 0.12 and 0.09, respectively. There are two main reasons for the discrepancy with ours. First, and more importantly, linear BAO is used in their modeling. In fact their constraints are similar to our R10k2 results shown in Table 2 because the BAO damping can be neglected at such high redshift. At low redshifts such as the MeerKAT redshift, the radial BAO feature is significantly damped (the transverse BAO is already damped by the beam), and this causes the radial BAO constraint to be weakened. Second, we include higher multipoles beyond the quadrupole.

In Villaescusa-Navarro et al. (2017), the radial power spectrum P_{\parallel} was used to forecast the BAO constraint for SKA-mid. They derive $(S/N)^2$ of 9990, while our radial correlation function $\xi_{r\parallel}$ yields $(S/N)^2 = 27800$. Our higher $(S/N)^2$ can be attributed to the fact that $\xi_{r\parallel}$ has been optimized with respect to $r_{\perp\max}$.

While our forecasts are still idealistic, e.g., the Gaussian beam approximation and the assumption that there are no residuals after foreground removal except the suppression of the modes by Eq. (6), nonetheless our model have captured the essence of these two important observational effects. With the (minor) differences in the forecast implementations in mind, our results broadly agree with others', and seem to suggest that our optimized statistics yield more attractive constraints. Our work can serve a useful guide to these experiments to further strengthen their constraining power.

6. CONCLUSIONS

There are a number of ongoing and forthcoming experiments aiming to measure the BAO using the 21 cm signals in the late universe. In this work we study the methods for 21 cm IM BAO measurement in configuration space using mocks and theory, with the focus on the 21 cm IM observational effects caused by the beam and foreground removal. We systematically compare the performance of three types of correlation functions for 21 cm IM BAO recovery, including the radial correlation function, multipole correlation function, and μ -wedge correlation function. Although these statistics are known in the literature, a quantitative comparison of their efficacy in BAO recovery was lacking and it is the goal of this paper to fill this gap.

The telescope beam and foreground removal effects are unique to 21 cm IM observation and can induce strong anisotropies in the correlation function. The beam smooths the correlation function in the transverse direction and we model its form as Gaussian. The foreground removal effect is a consequence of 21 cm foreground cleaning, and it sup-

presses the long wavelength modes in the radial direction. In particular, these effects cause strong artifacts in the transverse and radial axes, respectively, and we discuss their formation using some simple analytic models in Sec. 2.1.

We develop a BAO fitting pipeline for each of these correlation function estimators. The theory templates are presented in Sec. 2, and we derive their theory Gaussian covariance in Sec. 3. To verify and calibrate our pipeline, we make use of the H_I simulation from Avila et al. (2022). The mock catalogs use SAM simulations to model baryon and galaxy properties. The final H_I is obtained by post-processing the cold gas from the SAM simulation. From this 21 cm IM mock, we further add the beam and foreground removal effects.

We use the catalog to look for the optimal parameter choices for the three types of correlation functions under various observation conditions. For the radial correlation function $\xi_{r\parallel}$, we find that the BAO constraints tighten mildly with the transverse averaging scale, $r_{\perp\max}$. The constraints saturate at large $r_{\perp\max} \sim 50 \text{ Mpc } h^{-1}$, roughly independent of the R_{beam} and k_{fg} values, and thus we adopt $r_{\perp\max} = 50 \text{ Mpc } h^{-1}$ in defining $\xi_{r\parallel}$. For the multipole correlation function, when the quadrupole is added to the monopole, the constraint tightens substantially. They are further strengthened albeit with increasingly diminishing marginal return when the hexadecapole and hexacontatetrapole are also included. We consider the combination of monopole, quadrupole, hexadecapole and hexacontatetrapole in our analysis. The μ -wedge correlation function allows the flexibility to cut out some problematic regions. This is especially advantageous to the 21 cm IM correlation function as the strong artifacts caused by the observational effects are well localized in the regions close to the axes. By removing both ends, i.e., μ close to 1 and near 0, although the error bars are enlarged, robust BAO constraints can be derived. To achieve high signal-to-noise, we further divide the μ -range into multiple wedges to enhance the resolution. We find that with these strategies, these statistics achieve robust and consistent constraints across various observation conditions. (Fig. 9).

We apply the statistics with the optimal settings to forecast the BAO constraints for the 21 cm IM experiments including BINGO, MeerKAT, and SKA (Table 5 and Fig. 10). We find that for the low redshift experiments BINGO and MeerKAT, μ -wedge correlation function achieves the tightest constraint for both α_{\perp} and α_{\parallel} . For SKA-mid, the radial correlation function delivers the tightest constraint on α_{\parallel} , while the μ -wedge correlation function gives the smallest error bars on α_{\perp} . Although our analyses are still idealistic, our model captures the essence of the beam and foreground removal effects, and our results are expected to be a useful guide for these experiments.

ACKNOWLEDGMENTS

ZZ and KCC acknowledge the support by the National Science Foundation of China under the grant number 12273121 and 12533002, and the science research grant from the China Manned Space Project with CMS-CSST-2025-A02. SA has been funded by MCIN/AEI/10.13039/501100011033 and

FSE+ (Europe) under project PID2024-156844NA-C22 and the RYC2022-037311-I fellowship. BVG would like to acknowledge the support from the European Union (ERC StG, LSS BeyondAverage, 101075919) and the Comunidad de Madrid 2019-T1/TIC-12702 grant.

REFERENCES

- Abbott, T. M. C., Abdalla, F. B., Alarcon, A., et al. 2019, *MNRAS*, 483, 4866, doi: [10.1093/mnras/sty3351](https://doi.org/10.1093/mnras/sty3351)
- Abbott, T. M. C., Agüena, M., Allam, S., et al. 2022, *PhRvD*, 105, 043512, doi: [10.1103/PhysRevD.105.043512](https://doi.org/10.1103/PhysRevD.105.043512)
- Abbott, T. M. C., Adamow, M., Agüena, M., et al. 2024, *PhRvD*, 110, 063515, doi: [10.1103/PhysRevD.110.063515](https://doi.org/10.1103/PhysRevD.110.063515)
- Abdalla, E., Ferreira, E. G. M., Landim, R. G., et al. 2022, *A&A*, 664, A14, doi: [10.1051/0004-6361/202140883](https://doi.org/10.1051/0004-6361/202140883)
- Abdul Karim, M., Aguilar, J., Ahlen, S., et al. 2025, *PhRvD*, 112, 083515, doi: [10.1103/tr6y-kpc6](https://doi.org/10.1103/tr6y-kpc6)
- Adame, A. G., Aguilar, J., Ahlen, S., et al. 2025, *JCAP*, 2025, 021, doi: [10.1088/1475-7516/2025/02/021](https://doi.org/10.1088/1475-7516/2025/02/021)
- Alam, S., Ata, M., Bailey, S., et al. 2017, *MNRAS*, 470, 2617, doi: [10.1093/mnras/stx721](https://doi.org/10.1093/mnras/stx721)
- Alam, S., et al. 2021, *Phys. Rev. D*, 103, 083533, doi: [10.1103/PhysRevD.103.083533](https://doi.org/10.1103/PhysRevD.103.083533)
- Alonso, D., Bull, P., Ferreira, P. G., & Santos, M. G. 2015, *MNRAS*, 447, 400, doi: [10.1093/mnras/stu2474](https://doi.org/10.1093/mnras/stu2474)
- Amiri, M., Bandura, K., Chakraborty, A., et al. 2024, *ApJ*, 963, 23, doi: [10.3847/1538-4357/ad0f1d](https://doi.org/10.3847/1538-4357/ad0f1d)
- Anderson, C. J., Luciw, N. J., Li, Y.-C., et al. 2018, *MNRAS*, 476, 3382, doi: [10.1093/mnras/sty346](https://doi.org/10.1093/mnras/sty346)
- Anderson, L., et al. 2012, *MNRAS*, 427, 3435, doi: [10.1111/j.1365-2966.2012.22066.x](https://doi.org/10.1111/j.1365-2966.2012.22066.x)
- Angulo, R. E., & Pontzen, A. 2016, *MNRAS*, 462, L1, doi: [10.1093/mnras/1slw098](https://doi.org/10.1093/mnras/1slw098)
- Avila, S., Vos-Ginés, B., et al. 2022, *MNRAS*, 510, 292, doi: [10.1093/mnras/stab3406](https://doi.org/10.1093/mnras/stab3406)
- Battye, R. A., Browne, I. W. A., Dickinson, C., et al. 2013, *MNRAS*, 434, 1239, doi: [10.1093/mnras/stt1082](https://doi.org/10.1093/mnras/stt1082)
- Behroozi, P. S., Wechsler, R. H., & Wu, H.-Y. 2013a, *ApJ*, 762, 109, doi: [10.1088/0004-637X/762/2/109](https://doi.org/10.1088/0004-637X/762/2/109)
- Behroozi, P. S., Wechsler, R. H., Wu, H.-Y., et al. 2013b, *ApJ*, 763, 18, doi: [10.1088/0004-637X/763/1/18](https://doi.org/10.1088/0004-637X/763/1/18)
- Beutler, F., Blake, C., Colless, M., et al. 2011, *MNRAS*, 416, 3017, doi: [10.1111/j.1365-2966.2011.19250.x](https://doi.org/10.1111/j.1365-2966.2011.19250.x)
- Bharadwaj, S., Nath, B. B., & Sethi, S. K. 2001, *Journal of Astrophysics and Astronomy*, 22, 21, doi: [10.1007/BF02933588](https://doi.org/10.1007/BF02933588)
- Bond, J. R., & Efstathiou, G. 1984, *ApJL*, 285, L45, doi: [10.1086/184362](https://doi.org/10.1086/184362)
- . 1987, *MNRAS*, 226, 655, doi: [10.1093/mnras/226.3.655](https://doi.org/10.1093/mnras/226.3.655)
- Braun, R., Bourke, T., Green, J. A., Keane, E., & Wagg, J. 2015, in *Advancing Astrophysics with the Square Kilometre Array (AASKA14)*, 174, doi: [10.22323/1.215.0174](https://doi.org/10.22323/1.215.0174)
- Bull, P., Ferreira, P. G., Patel, P., & Santos, M. G. 2015, *ApJ*, 803, 21, doi: [10.1088/0004-637X/803/1/21](https://doi.org/10.1088/0004-637X/803/1/21)
- Chan, K. C., Crocce, M., Ross, A. J., et al. 2018, *MNRAS*, 480, 3031, doi: [10.1093/mnras/sty2036](https://doi.org/10.1093/mnras/sty2036)
- Chan, K. C., Avila, S., Carnero Rosell, A., et al. 2022, *PhRvD*, 106, 123502, doi: [10.1103/PhysRevD.106.123502](https://doi.org/10.1103/PhysRevD.106.123502)
- Chang, T.-C., Pen, U.-L., Bandura, K., & Peterson, J. B. 2010, *Nature*, 466, 463, doi: [10.1038/nature09187](https://doi.org/10.1038/nature09187)
- Chang, T.-C., Pen, U.-L., Peterson, J. B., & McDonald, P. 2008, *PhRvL*, 100, 091303, doi: [10.1103/PhysRevLett.100.091303](https://doi.org/10.1103/PhysRevLett.100.091303)
- CHIME Collaboration, Amiri, M., Bandura, K., et al. 2025, arXiv e-prints, arXiv:2511.19620, doi: [10.48550/arXiv.2511.19620](https://doi.org/10.48550/arXiv.2511.19620)
- Chuang, C.-H., Yepes, G., Kitaura, F.-S., et al. 2019, *MNRAS*, 487, 48, doi: [10.1093/mnras/stz1233](https://doi.org/10.1093/mnras/stz1233)
- Cole, S., Percival, W. J., Peacock, J. A., et al. 2005, *MNRAS*, 362, 505, doi: [10.1111/j.1365-2966.2005.09318.x](https://doi.org/10.1111/j.1365-2966.2005.09318.x)
- Crocce, M., & Scoccimarro, R. 2006, *PhRvD*, 73, 063519, doi: [10.1103/PhysRevD.73.063519](https://doi.org/10.1103/PhysRevD.73.063519)
- Croton, D. J., Stevens, A. R. H., Tonini, C., et al. 2016, *ApJS*, 222, 22, doi: [10.3847/0067-0049/222/2/22](https://doi.org/10.3847/0067-0049/222/2/22)
- Cunnington, S., Irfan, M. O., Carucci, I. P., Pourtsidou, A., & Bobin, J. 2021, *MNRAS*, 504, 208, doi: [10.1093/mnras/stab856](https://doi.org/10.1093/mnras/stab856)
- Cunnington, S., Li, Y., Santos, M. G., et al. 2023, *MNRAS*, 518, 6262, doi: [10.1093/mnras/stac3060](https://doi.org/10.1093/mnras/stac3060)
- Dodelson, S. 2003, *Modern cosmology* (Amsterdam: Academic Press)
- Eisenstein, D. J., Zehavi, I., Hogg, D. W., et al. 2005, *ApJ*, 633, 560, doi: [10.1086/466512](https://doi.org/10.1086/466512)
- Foreman-Mackey, D., Hogg, D. W., Lang, D., & Goodman, J. 2013, *Publications of the Astronomical Society of the Pacific*, 125, 306, doi: [10.1086/670067](https://doi.org/10.1086/670067)
- Furlanetto, S. R., Oh, S. P., & Briggs, F. H. 2006, *PhR*, 433, 181, doi: [10.1016/j.physrep.2006.08.002](https://doi.org/10.1016/j.physrep.2006.08.002)
- Gaztanaga, E., Cabre, A., & Hui, L. 2009, *MNRAS*, 399, 1663, doi: [10.1111/j.1365-2966.2009.15405.x](https://doi.org/10.1111/j.1365-2966.2009.15405.x)
- Hu, W., & Sugiyama, N. 1996, *ApJ*, 471, 542, doi: [10.1086/177989](https://doi.org/10.1086/177989)
- Hu, W., Sugiyama, N., & Silk, J. 1997, *Nature*, 386, 37, doi: [10.1038/386037a0](https://doi.org/10.1038/386037a0)

- Hyvarinen, A. 1999, *IEEE Transactions on Neural Networks*, 10, 626, doi: [10.1109/72.761722](https://doi.org/10.1109/72.761722)
- Ivanov, M. M., & Sibiryakov, S. 2018, *JCAP*, 2018, 053, doi: [10.1088/1475-7516/2018/07/053](https://doi.org/10.1088/1475-7516/2018/07/053)
- Kazin, E. A., Koda, J., Blake, C., et al. 2014, *MNRAS*, 441, 3524, doi: [10.1093/mnras/stu778](https://doi.org/10.1093/mnras/stu778)
- Kennedy, F., & Bull, P. 2021, *MNRAS*, 506, 2638, doi: [10.1093/mnras/stab1814](https://doi.org/10.1093/mnras/stab1814)
- Knebe, A., Stoppacher, D., Prada, F., et al. 2018, *MNRAS*, 474, 5206, doi: [10.1093/mnras/stx2662](https://doi.org/10.1093/mnras/stx2662)
- Knebe, A., Lopez-Cano, D., Avila, S., et al. 2022, *MNRAS*, 510, 5392, doi: [10.1093/mnras/stac006](https://doi.org/10.1093/mnras/stac006)
- Lewis, A., Challinor, A., & Lasenby, A. 2000, *ApJ*, 538, 473, doi: [10.1086/309179](https://doi.org/10.1086/309179)
- Li, Q., Wang, X., Li, X.-D., et al. 2025, *JCAP*, 2025, 082, doi: [10.1088/1475-7516/2025/04/082](https://doi.org/10.1088/1475-7516/2025/04/082)
- Liu, A., & Shaw, J. R. 2020, *PASP*, 132, 062001, doi: [10.1088/1538-3873/ab5bfd](https://doi.org/10.1088/1538-3873/ab5bfd)
- Loeb, A., & Wyithe, J. S. B. 2008, *PhRvL*, 100, 161301, doi: [10.1103/PhysRevLett.100.161301](https://doi.org/10.1103/PhysRevLett.100.161301)
- Maartens, R., Abdalla, F. B., Jarvis, M., & Santos, M. G. 2015, in *Advancing Astrophysics with the Square Kilometre Array (AASKA14)*, 16, doi: [10.22323/1.215.0016](https://doi.org/10.22323/1.215.0016)
- Mao, Y., Tegmark, M., McQuinn, M., Zaldarriaga, M., & Zahn, O. 2008, *PhRvD*, 78, 023529, doi: [10.1103/PhysRevD.78.023529](https://doi.org/10.1103/PhysRevD.78.023529)
- Masui, K. W., Switzer, E. R., Banavar, N., et al. 2013, *ApJL*, 763, L20, doi: [10.1088/2041-8205/763/1/L20](https://doi.org/10.1088/2041-8205/763/1/L20)
- McQuinn, M., Zahn, O., Zaldarriaga, M., Hernquist, L., & Furlanetto, S. R. 2006, *ApJ*, 653, 815, doi: [10.1086/505167](https://doi.org/10.1086/505167)
- Mead, A. J., Brieden, S., Tröster, T., & Heymans, C. 2021, *MNRAS*, 502, 1401, doi: [10.1093/mnras/stab082](https://doi.org/10.1093/mnras/stab082)
- Novaes, C. P., Zhang, J., de Mericia, E. J., et al. 2022, *A&A*, 666, A83, doi: [10.1051/0004-6361/202243158](https://doi.org/10.1051/0004-6361/202243158)
- Paul, S., Santos, M. G., Chen, Z., & Wolz, L. 2023, arXiv e-prints, arXiv:2301.11943, doi: [10.48550/arXiv.2301.11943](https://doi.org/10.48550/arXiv.2301.11943)
- Peebles, P. J. E., & Yu, J. T. 1970, *ApJ*, 162, 815, doi: [10.1086/150713](https://doi.org/10.1086/150713)
- Planck Collaboration, Ade, P. A. R., Aghanim, N., et al. 2016, *A&A*, 594, A13, doi: [10.1051/0004-6361/201525830](https://doi.org/10.1051/0004-6361/201525830)
- Pritchard, J. R., & Loeb, A. 2008, *PhRvD*, 78, 103511, doi: [10.1103/PhysRevD.78.103511](https://doi.org/10.1103/PhysRevD.78.103511)
- . 2012, *Reports on Progress in Physics*, 75, 086901, doi: [10.1088/0034-4885/75/8/086901](https://doi.org/10.1088/0034-4885/75/8/086901)
- Sánchez, A. G., Kazin, E. A., Beutler, F., et al. 2013, *MNRAS*, 433, 1202, doi: [10.1093/mnras/stt799](https://doi.org/10.1093/mnras/stt799)
- Santos, M., Bull, P., Alonso, D., et al. 2015, in *Advancing Astrophysics with the Square Kilometre Array (AASKA14)*, 19, doi: [10.22323/1.215.0019](https://doi.org/10.22323/1.215.0019)
- Santos, M., Bull, P., Camera, S., et al. 2016, in *MeerKAT Science: On the Pathway to the SKA*, 32, doi: [10.22323/1.277.0032](https://doi.org/10.22323/1.277.0032)
- Seo, H.-J., Ho, S., White, M., et al. 2012, *ApJ*, 761, 13, doi: [10.1088/0004-637X/761/1/13](https://doi.org/10.1088/0004-637X/761/1/13)
- Smith, R. E., Peacock, J. A., Jenkins, A., et al. 2003, *MNRAS*, 341, 1311, doi: [10.1046/j.1365-8711.2003.06503.x](https://doi.org/10.1046/j.1365-8711.2003.06503.x)
- Soares, P. S., Cunnington, S., Pourtsidou, A., & Blake, C. 2021, *MNRAS*, 502, 2549, doi: [10.1093/mnras/stab027](https://doi.org/10.1093/mnras/stab027)
- Springel, V. 2005, *MNRAS*, 364, 1105, doi: [10.1111/j.1365-2966.2005.09655.x](https://doi.org/10.1111/j.1365-2966.2005.09655.x)
- Square Kilometre Array Cosmology Science Working Group, Bacon, D. J., Battye, R. A., et al. 2020, *PASA*, 37, e007, doi: [10.1017/pasa.2019.51](https://doi.org/10.1017/pasa.2019.51)
- Sunyaev, R. A., & Zeldovich, Y. B. 1970, *Astrophysics and Space Science*, 7, 3, doi: [10.1007/BF00653471](https://doi.org/10.1007/BF00653471)
- Tansella, V., Jelic-Cizmek, G., Bonvin, C., & Durrer, R. 2018, *JCAP*, 2018, 032, doi: [10.1088/1475-7516/2018/10/032](https://doi.org/10.1088/1475-7516/2018/10/032)
- Thompson, A. R., Moran, J. M., & Swenson, G. W. 2017, *Interferometry and synthesis in radio astronomy (John Wiley & Sons, Ltd)*
- Villaescusa-Navarro, F., Alonso, D., & Viel, M. 2017, *MNRAS*, 466, 2736, doi: [10.1093/mnras/stw3224](https://doi.org/10.1093/mnras/stw3224)
- Wolz, L., Abdalla, F. B., Blake, C., et al. 2014, *MNRAS*, 441, 3271, doi: [10.1093/mnras/stu792](https://doi.org/10.1093/mnras/stu792)
- Wolz, L., Pourtsidou, A., Masui, K. W., et al. 2022, *MNRAS*, 510, 3495, doi: [10.1093/mnras/stab3621](https://doi.org/10.1093/mnras/stab3621)
- Wuensche, C. A., Villela, T., Abdalla, E., et al. 2022, *A&A*, 664, A15, doi: [10.1051/0004-6361/202039962](https://doi.org/10.1051/0004-6361/202039962)
- Xu, X., Padmanabhan, N., Eisenstein, D. J., Mehta, K. T., & Cuesta, A. J. 2012, *MNRAS*, 427, 2146, doi: [10.1111/j.1365-2966.2012.21573.x](https://doi.org/10.1111/j.1365-2966.2012.21573.x)
- Zoldan, A., De Lucia, G., Xie, L., Fontanot, F., & Hirschmann, M. 2017, *MNRAS*, 465, 2236, doi: [10.1093/mnras/stw2901](https://doi.org/10.1093/mnras/stw2901)